

# Reversible C–C Bond Formation between Redox-Active Pyridine Ligands in Iron Complexes

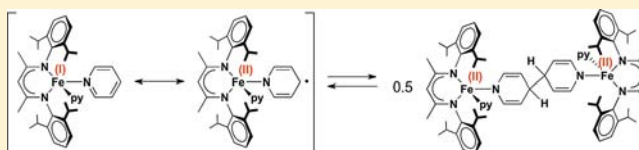
Thomas R. Dugan,<sup>†</sup> Eckhard Bill,<sup>‡</sup> K. Cory MacLeod,<sup>†</sup> Gemma J. Christian,<sup>‡</sup> Ryan E. Cowley,<sup>†</sup> William W. Brennessel,<sup>†</sup> Shengfa Ye,<sup>‡</sup> Frank Neese,<sup>\*,‡</sup> and Patrick L. Holland<sup>\*,†</sup>

<sup>†</sup>Department of Chemistry, University of Rochester, Rochester, New York

<sup>‡</sup>Max Planck Institute for Chemical Energy Conversion, Mülheim an der Ruhr, Germany

## Supporting Information

**ABSTRACT:** This manuscript describes the formally iron(I) complexes  $L^{Me}Fe(Py-R)_2$  ( $L^{Me}$  = bulky  $\beta$ -diketiminate; R = H, 4-*t*Bu), in which the basal pyridine ligands preferentially accept significant unpaired spin density. Structural, spectroscopic, and computational studies on the complex with 4-*tert*-butylpyridine (<sup>t</sup>Bu<sub>4</sub>py) indicate that the  $S = 3/2$  species is a resonance hybrid between descriptions as (a) high-spin iron(II) with antiferromagnetic coupling to a pyridine anion radical and (b) high-spin iron(I). When the pyridine lacks the protection of the *tert*-butyl group, it rapidly and reversibly undergoes radical coupling reactions that form new C–C bonds. In one reaction, the coordinated pyridine couples to triphenylmethyl radical, and in another, it dimerizes to give a pyridine-derived dianion that bridges two iron(II) ions. The rapid, reversible C–C bond formation in the dimer stores electrons from the formally reduced metal as a C–C bond in the ligands, as demonstrated by using the coupled diiron(II) complex to generate products that are known to come from iron(I) precursors.



## INTRODUCTION

Recent years have seen a burst of activity in the use of ligands that are “noninnocent”, because they can undergo reversible changes that facilitate reactions. Most often, these changes indicate *redox* noninnocence: for example, in reduced complexes, the ligand can accept excess charge from the metal through an internal electron-transfer event.<sup>1</sup> Polypyridines are one of the seminal types of electron-accepting ligands.<sup>2</sup> Consequently, the electrochemistry, photochemistry, and bonding interactions of redox-active bipyridine metal complexes have been thoroughly examined.<sup>3</sup> Recent attention has also focused on related systems with supporting ligands that combine pyridines with other conjugated *N*-donors.<sup>4</sup>

A less common form of ligand noninnocence involves reversible bond formation within ligands. The reversible formation of a bond can “store” the electrons from redox noninnocence. For example, Nocera has reported that porphyrinogen can store electrons through the reversible formation of C–C bonds (Figure 1).<sup>5</sup> Wolczanski has reported reversible double C–C bond formations between bis(2-pyridyl-azaallyl) ligands.<sup>6</sup>

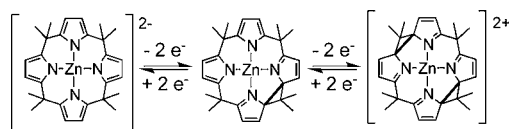


**Figure 1.** An example of reversible C–C bond formation at a porphyrinogen ligand.<sup>5</sup>

The work reported here utilizes pyridine as the key redox-active ligand. Pyridine can be reduced to its radical anion (Figure 2) at the very cathodic potential of  $-2.7$  V vs SCE.<sup>7</sup> Despite the demonstrations of polypyridine reduction, simple pyridine ligands have rarely been reported to attain their radical anion forms in transition metal complexes. A few examples of redox-active pyridine ligands use electron-withdrawing groups to stabilize the ligand-based radical<sup>13,8</sup> or are equipped with redox-active tetrathiafulvalene groups.<sup>9</sup>

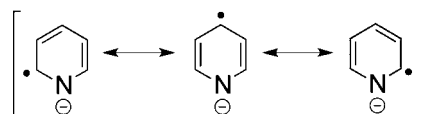


**Figure 2.** Dominant resonance structures of a pyridine radical anion.

There are a number of complexes in which a reduced polypyridine ligand undergoes an *irreversible* C–C bond formation that is suggestive of ligand radical character.<sup>10</sup> There are fewer examples of this irreversible reductive coupling with monodentate pyridine ligands.<sup>11–13</sup> To our knowledge, there are no literature examples in which a C–C coupling reaction from a redox-active pyridine in a transition-metal complex has been demonstrated to be reversible.

In this report, iron  $\beta$ -diketiminate complexes of pyridine and 4-*tert*-butylpyridine are isolated and characterized in detail. A combination of crystallography, spectroscopy, reactivity, and

Received: June 12, 2012

Published: November 26, 2012

computations shows that a pyridine ligand in the complex accepts an unpaired electron from the metal. Most importantly, the pyridine complex undergoes a rapid, reversible C–C bond forming reaction between radical pyridine ligands. The product has electrons stored in a ligand-based C–C bond, and these electrons may be returned to the metal for use in further reactions.

## RESULTS

### Formation of a Mononuclear Iron–Pyridine Complex.

The iron dinitrogen complex  $L^{\text{Me}}\text{FeNNFe}L^{\text{Me}}$  ( $L^{\text{Me}} = 2,4$ -bis(2,6-diisopropylimino)pentyl) and the benzene complex  $L^{\text{Me}}\text{Fe}(\eta^6\text{-benzene})$  are convenient sources of the iron(I) fragment  $L^{\text{Me}}\text{Fe}$ .<sup>14</sup> Addition of two or more equivalents of 4-*tert*-butylpyridine ( $t^{\text{Bu}}\text{py}$ ) to a solution of  $L^{\text{Me}}\text{Fe}(\eta^6\text{-benzene})$  in pentane or addition of four or more equivalents of  $t^{\text{Bu}}\text{py}$  to a solution of  $L^{\text{Me}}\text{FeNNFe}L^{\text{Me}}$  in pentane produces a dark green solution. The product,  $L^{\text{Me}}\text{Fe}(t^{\text{Bu}}\text{py})_2$  (**1**), may be isolated in 82% yield using either method. The X-ray crystal structure of **1** shows two independent molecules in the asymmetric unit; they are nearly identical and one of them is shown in Figure 3. This is the first crystallographically characterized pyridine complex of a formally iron(I) ion.<sup>15,16</sup>

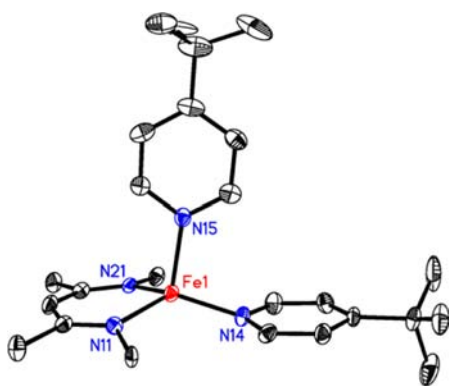


**Figure 3.** Molecular structure of  $L^{\text{Me}}\text{Fe}(t^{\text{Bu}}\text{py})_2$  (**1**), using 50% thermal ellipsoids. The 2,6-diisopropylaryl groups and hydrogen atoms have been removed for clarity. Only one of the two molecules in the asymmetric unit is shown. Selected bond distances (Å) and bond angles (deg): Fe1–N14, 1.936(4); Fe1–N15, 2.058(4); Fe1–N11, 1.989(4); Fe1–N21, 1.982(4); N14–Fe1–N15, 98.8(2); N11–Fe1–N14, 121.7(2); N21–Fe1–N14, 127.4(2); N21–Fe1–N11, 96.1(2); N11–Fe1–N15, 108.3(2); N21–Fe1–N15, 102.4(2).

In **1**, the apical Fe– $N_{\text{py}}$  bond distances are 2.058(4) and 2.070(4) Å, and the basal Fe– $N_{\text{py}}$  bond distances are 1.936(4) and 1.930(4) Å. All of these Fe– $N_{\text{py}}$  distances are at least one standard deviation shorter than the average of iron complexes of monodentate pyridines in the Cambridge Structural Database, and the basal Fe– $N_{\text{py}}$  bond distances are significantly (0.03 Å) shorter than *any* reported Fe– $N_{\text{py}}$  bond distance.<sup>17</sup> This suggests that the basal pyridine resembles an anionic amido ligand, as shown in the right-hand resonance structure in Figure 4.

The structural parameters within the pyridine ligands of **1** are also consistent with distortion toward a  $t^{\text{Bu}}\text{py}^{\bullet-}$  formulation. The C–N bond distances in the basal  $t^{\text{Bu}}\text{py}$  ligand are significantly longer than in free 4-*tert*-butylpyridine (Figure 5). The distortions are almost as extensive as those in the radical anion of pyridine but do not indicate complete one-

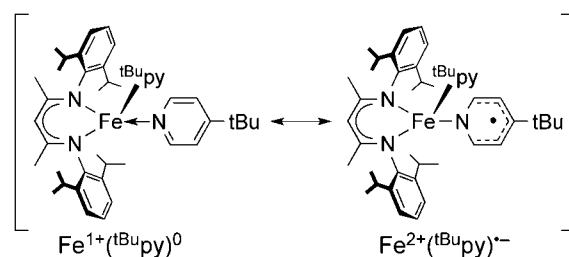


**Figure 4.** Two resonance structures for compound **1**. On the left is an iron(I) resonance structure, and the right resonance structure shows an anionic pyridine radical in the basal position of an iron(II) complex.

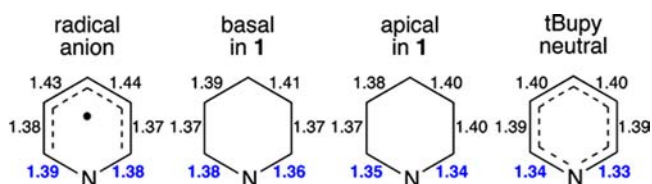


**Figure 5.** Comparison of the distances within the pyridine rings in the crystal structure of **1** (labeled “basal” and “apical”) to those in the B3LYP/TZVP geometry-optimized structures of  $t^{\text{Bu}}\text{py}$  (right) and its radical anion (left). The highlighted C–N distances show the largest difference in bond length between  $t^{\text{Bu}}\text{py}$  and  $t^{\text{Bu}}\text{py}^{\bullet-}$ . Uncertainties in the crystallographically determined bond distances in **1** are less than 0.01 Å.

electron reduction. The distortion of the apical pyridine in **1** is much less than in the basal pyridine. This structural measure further supports the assignment of the basal pyridine ligand as having radical anion character.

**Spectroscopic and Magnetic Characterization of  $L^{\text{Me}}\text{Fe}(t^{\text{Bu}}\text{py})_2$ .** The X-ray crystal structure of compound **1** has pseudo- $C_s$  symmetry, with an approximate mirror plane bisecting both the  $N_2C_3\text{Fe}$  plane and the basal  $t^{\text{Bu}}\text{py}$  and containing the apical  $t^{\text{Bu}}\text{py}$  (see Figures 3 and 4 above). However, the  $^1\text{H}$  NMR spectrum of **1** in  $C_6D_6$  indicates averaged  $C_{2v}$  symmetry in solution, with nine paramagnetically shifted resonances (three for  $t^{\text{Bu}}\text{py}$  and six for the  $\beta$ -diketiminato). The higher symmetry of **1** in solution is attributed to movement of the  $t^{\text{Bu}}\text{py}$  ligands between apical and basal positions rapidly on the  $^1\text{H}$  NMR time scale. The  $^1\text{H}$  NMR resonances do not shift in the presence of 10 equiv of  $t^{\text{Bu}}\text{py}$ , indicating that the  $t^{\text{Bu}}\text{py}$  ligands do not exchange with free *tert*-butylpyridine on the NMR time scale and that the basal/apical pyridine exchange is intramolecular.

The distinctive electronic absorption spectrum of **1** in hexane is shown in Figure 6. The solid state and solution electronic absorption spectra of **1** are indistinguishable. The most prominent features are intense low-energy bands at  $\lambda_{\text{max}} = 847$  nm ( $\epsilon = 6400 \text{ M}^{-1}\text{cm}^{-1}$ ) and  $\lambda_{\text{max}} = 1245$  nm ( $\epsilon = 5600 \text{ M}^{-1}\text{cm}^{-1}$ ). A Gaussian fit to the low-energy region (Figure 10 below) indicates that these correspond to electronic transitions at  $11678 \text{ cm}^{-1}$  ( $f_{\text{osc}} = 0.010$ ) and  $7606 \text{ cm}^{-1}$  ( $f_{\text{osc}} = 0.071$ ). The intense low-energy transitions have been observed in complexes of bipyridine radical ligands and are typically attributed to a ligand–ligand charge transfer (LLCT) or a  $\pi$ – $\pi^*$  transition within a radical anion ligand.<sup>3,18,19</sup> The assignments for the bands in **1** will be explored in more detail below using computations.

Solid-state magnetic susceptibility studies of solid **1** at 1 T (Figure S1, Supporting Information) give a magnetic moment near  $3.7 \mu_B$  above 100 K, which is close to the expected  $3.9 \mu_B$

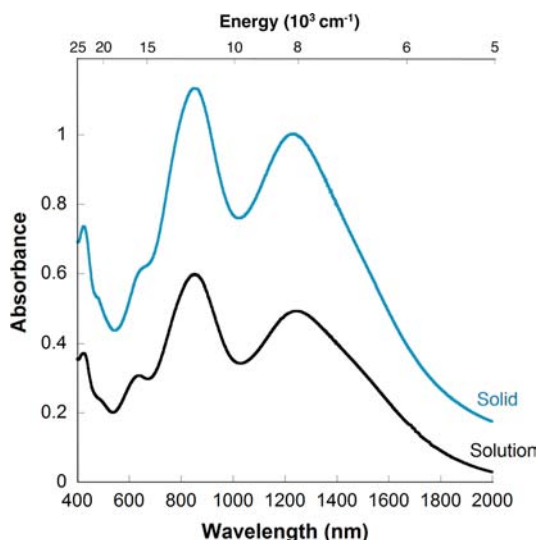


**Figure 6.** The electronic absorption spectrum of  $L^{\text{Me}}\text{Fe}(\text{tBu}_p\text{py})_2$  (**1**) in the solid state (blue line) and in hexane solution (black line). A spectrum on a linear energy scale with Gaussian fits is given in the Supporting Information.

for an  $S = 3/2$  paramagnet. At lower temperatures, the magnetic moment decreases due to zero-field splitting. Temperature- and field-dependent susceptibility data could be simulated with an axial zero-field splitting parameter of  $D = -8 \text{ cm}^{-1}$  (Figure S1, Supporting Information). The quartet spin state ( $S = 3/2$ ) is also evident from the derivative X-band EPR spectrum of **1** recorded in frozen toluene/benzene solution at several temperatures (Figure 7). The spectrum is dominated by a sharp peak at  $g_{\text{eff}} \approx 6$  (labeled Y1) and a broad derivative line centered below  $g_{\text{eff}} = 2$ . The features can be assigned to the  $m_S = \pm 3/2$  Kramers doublet of an  $S = 3/2$  system with large zero-field splitting and high rhombicity ( $E/D$ ). A second peak at  $g_{\text{eff}}$

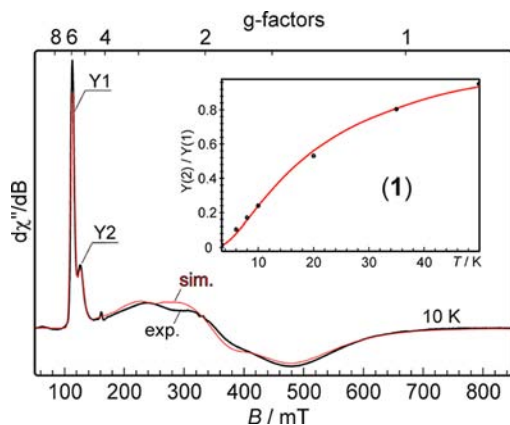


**Figure 7.** X-band EPR spectrum of  $L^{\text{Me}}\text{Fe}(\text{tBu}_p\text{py})_2$  (**1**) recorded in 3:1 (v/v) toluene/benzene glass at 10 K. Parameters: microwave frequency 9.386 GHz, microwave power 20  $\mu\text{W}$ , modulation 1 mT/100 kHz, time constant 82 ms. The red line represents a spin Hamiltonian simulation for  $S = 3/2$  with  $D = -5.9 \text{ cm}^{-1}$ ,  $E/D = 0.27$ , and  $\mathbf{g} = (2.147, 2.015, 2.116)$ . The line shape of the powder spectrum was obtained with a frequency-dependent Gaussian line width of 40 mT at  $g = 1$  and a Gaussian distribution of the rhombicity parameter with half width  $\sigma(E/D) = 0.052$ . The inset shows the intensity ratio of the peak amplitudes Y2/Y1 (black dots) and a fit with a Boltzmann function for the energy gap  $2D$  of the Kramers doublets ( $Y2/Y1 = \text{constant } e^{-2D/(kT)}$ , red line).

$\approx 5$  (Y2) is seen at temperatures above 4 K, which originates from thermal population of the second Kramers doublet  $m_S = \pm 1/2$  in a system with a negative zero-field splitting parameter  $D$ . The temperature dependence of the ratio of intensities Y2 and Y1 fits to  $D = -5.9 \text{ cm}^{-1}$  (inset of Figure 7), which compares well with the value from the susceptibility studies ( $-8 \text{ cm}^{-1}$ ). Simulations of the EPR spectra recorded at several temperatures are shown as red lines in Figure 7 and Figure S2, Supporting Information, and indicate that  $E/D = 0.27$  and intrinsic  $\mathbf{g} = (2.147, 2.015, 2.116)$ . These parameters indicate the presence of a nondegenerate orbital ground state.

It is interesting to compare these parameters to those for the four-coordinate tetrazene iron complex  $L^{\text{Me}}\text{Fe}(\text{AdN}(\text{NNN})\text{Ad})$  ( $S = 3/2$ ;  $D = -16 \text{ cm}^{-1}$ ;  $E/D = 0.06$ ), which was assigned as an iron(II) complex with a coordinated radical.<sup>20</sup> Both this complex and **1** have spin quartet ground states, characterized by large, negative zero-field splitting parameter  $D$ . The similar size and the same sign of  $D$  indicate similar ground states with low-lying excited states. The lower  $D$  in **1** presumably reflects slightly higher relative energies of the excited states (this also gives less extreme effective  $g_{\text{eff}}$  values in **1**, which make the EPR spectrum easier to detect than the highly anisotropic pattern for  $L^{\text{Me}}\text{Fe}(\text{AdN}(\text{NNN})\text{Ad})$ ). The only major difference is in the rhombicity of the zero-field splitting, which is higher in **1** (0.27 vs 0.06). The  $m_S = \pm 1/2$  Kramers doublet of the spin quartet can be observed for **1**, whereas the larger zero-field splitting prevented this in the more axial tetrazene complex. Overall, the spectroscopic features of **1** are similar to  $L^{\text{Me}}\text{Fe}(\text{AdN}(\text{NNN})\text{Ad})$ , and the different details can be explained by the change in the magnitude and rhombicity of zero-field splitting between the complexes.

The zero-field Mössbauer spectrum of a solid sample of **1** at 80 K has a quadrupole doublet with isomer shift  $\delta = 0.79 \text{ mm/s}$  and quadrupole splitting  $|\Delta E_Q| = 0.59 \text{ mm/s}$  (Figure 8). The asymmetry of the spectrum is consistent with intermediate spin relaxation, which is common for paramagnetic compounds with

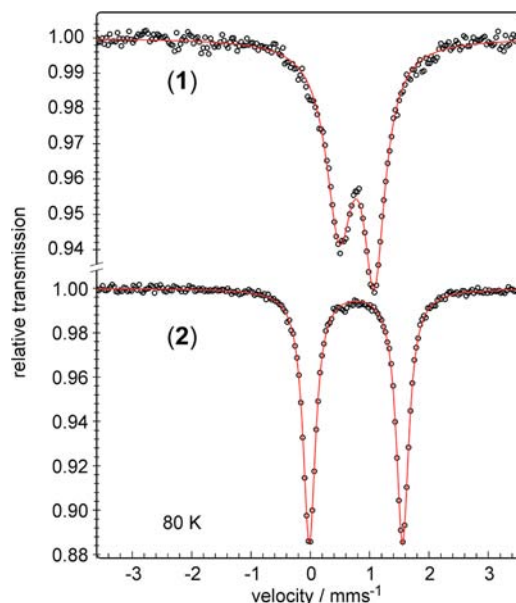


**Figure 8.** Zero-field Mössbauer spectra of  $L^{\text{Me}}\text{Fe}(\text{tBu}_p\text{py})_2$  (**1**) and  $\{\text{L}^{\text{Me}}\text{FePy}\}_2(\mu\text{-C}_{10}\text{H}_{10}\text{N}_2)$  (**2**) recorded at 80 K. The black circles are the data, and the red lines represent simulations of the spectra using the parameters in the text.

half-integer spin.<sup>20</sup> The isomer shift of **1** is close to that for the four-coordinate iron(I) complex  $L^{Me}Fe(NC^tBu)_2$  ( $\delta = 0.72$  mm/s)<sup>21</sup> but is also near the four-coordinate iron(II) complex  $\{L^{Me}Fe\}_2(N_6Ad_2)$  [ $N_6Ad_2 = 1,6$ -bis(1-adamantyl)-hexazadienyl] ( $\delta = 0.75$  mm/s).<sup>22</sup> It is also similar to the aforementioned tetrazene complex that was assigned as iron(II) with a coordinated radical ( $\delta = 0.69$  mm/s).<sup>20</sup> However, because the isomer shift ranges are similar for high-spin iron(I) and high-spin iron(II) compounds of  $\beta$ -diketiminates, this measure does not serve as a clear criterion for assignment of the oxidation state at the iron center.

**DFT Analysis of  $L^{Me}Fe(tBuPy)_2$ .** The electronic structure of **1** (using the crystallographic positions of all atoms) was examined with the ORCA suite of programs, using the TPSSh functional<sup>23</sup> with the SVP basis set on hydrogens and TZVP basis set on all other atoms.<sup>24</sup> Several functionals were tested, and TPSSh/TZVP was chosen because it accurately predicts the experimentally observed spectral features. The quartet state is calculated to be the ground state (the sextet and doublet states are higher in energy by at least 60 kcal/mol), in agreement with the experimentally determined magnetic moment and EPR spectra. The predicted<sup>25</sup> Mössbauer parameters of  $\delta = 0.76$  mm/s and  $|\Delta E_Q| = 0.53$  mm/s agree well with the experimental parameters ( $\delta = 0.79$  mm/s,  $|\Delta E_Q| = 0.59$  mm/s). The low-energy part of the UV-vis spectrum also has reasonable agreement with that predicted by TD-DFT computations at the same level of theory (see below).

The spectroscopically validated computational model at the crystallographic geometry of **1** indicates frontier orbitals in which most pairs of  $\alpha$  (spin-up) and  $\beta$  (spin-down) corresponding orbitals have an overlap of  $>0.95$ .<sup>26</sup> Figure 9 shows matching  $\alpha$  and  $\beta$  orbital pairs as single orbitals. In contrast, one pair of one-electron orbitals has a lower overlap of 0.89, and these corresponding orbitals are shown as adjacent horizontal lines. The low overlap suggests contribution from a ligand-based radical with the  $\beta$  spin on the ligand antiferromagnetically coupled to the four  $\alpha$  spins on a high-spin iron(II) center. This coupling leads to an overall quartet ( $S = 3/2$ ) ground state as observed experimentally.

The energy ordering of the frontier orbitals in Figure 9 is as expected for a pseudotetrahedral geometry. Though the orbital splitting of a tetrahedron is typically described with  $d_z^2$  and  $d_{x^2-y^2}$  as the low-lying orbitals, the axes in Figure 9 are rotated 45° from the  $S_4$  axis of a tetrahedron; this leads to the orbital labels found in the figure. The key orbital with a  $\beta$  spin (Figure 9, right) arises from  $\pi$ -bonding between the iron  $d_z^2$  orbital and the  $\pi^*$  LUMO of the basal  $tBuPy$  ligand. This  $\beta$  orbital is not completely ligand-localized; note that it has more than 50% metal character, and thus the DFT computations suggest an electronic structure that is best viewed as a resonance hybrid between iron(I)-pyridine and iron(II)-pyridine radical resonance structures in Figure 2. However, the pyridines clearly have radical character with an opposite spin to that on the metal: the Löwdin spin density is  $-0.27$  on the basal pyridine ligand, with  $-0.18 e^-$  of this on the *para* position (Figure 9, bottom).

Time-dependent DFT (TD-DFT) analysis of the same model predicts two intense low-energy electronic transitions at 10197  $cm^{-1}$  ( $f_{osc} = 0.082$ ) and 11823  $cm^{-1}$  ( $f_{osc} = 0.040$ ), in rough agreement with the observed bands at 7606 ( $f_{osc} = 0.071$ ) and 11678  $cm^{-1}$  ( $f_{osc} = 0.010$ ). Figure 10a shows the observed spectrum and Gaussian fits to the three major low-energy transitions, and Figure 10b shows the predicted

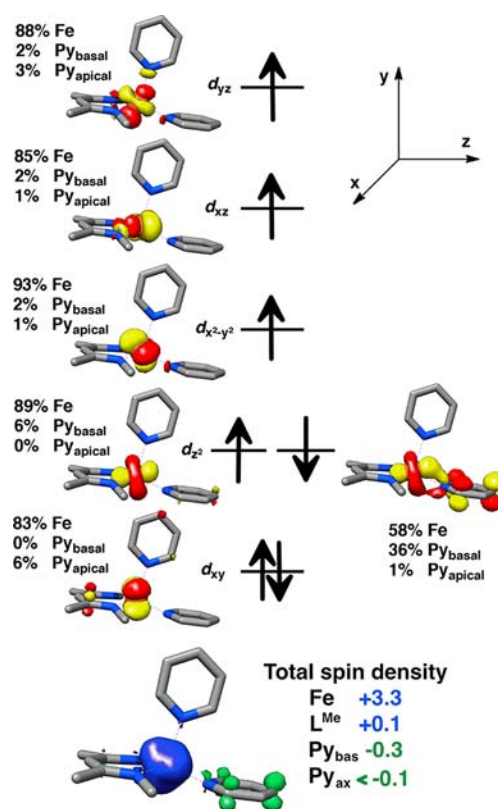


**Figure 9.** (top) Ligand-field quasi-restricted molecular orbitals from the DFT model of **1**, overlaid on the core of the molecule. The composition of each molecular orbital is shown. One  $\alpha$  (spin-up) and one  $\beta$  (spin-down) orbital have a relatively low spatial overlap of 0.89, and this  $\beta$  electron lies largely on the basal pyridine. (bottom) The basal pyridine has significant spin density with an opposite sign to that of the iron, implying a ligand radical with antiferromagnetic coupling to the metal spin.

transition energies with sticks indicating the oscillator strength of each transition. The predicted oscillator strengths give a predicted spectrum that has peaks of roughly the same size as the experimental spectrum (Figure 10c). The match between the predicted and experimental spectra is comparable to that seen in other systems.<sup>27</sup>

Tentative assignments of the bands to the most intense transitions are indicated by arrows connecting the data in Figure 10a to the predictions in Figure 10b. Each of the intense transitions has multiconfigurational character, and thus is not rigorously described by TD-DFT, further suggesting caution in the assignments.<sup>27</sup> With these caveats, we interpret the intense predicted bands using the difference densities between the ground-state and excited-state orbitals (Figure 11). The intense band calculated at 10198  $cm^{-1}$  has its largest contribution from  $d_{xy} \rightarrow$  apical  $py$  MLCT (69%), and the one at 11824  $cm^{-1}$  has contributions from multiple  $d-d$  transitions.<sup>28</sup> The higher-energy predicted band at 18585  $cm^{-1}$  is MLCT from the metal to the  $\pi$ -system of the  $\beta$ -diketimate ligand. The LLCT transition from the basal to apical pyridine is associated with the lowest-energy predicted transition at 6692  $cm^{-1}$  (1494 nm), but it has a much smaller predicted intensity ( $f_{osc} = 0.001$ ). An even smaller intensity ( $f_{osc} = 0.0001$ ) is predicted for MLCT to the basal pyridine (8749  $cm^{-1}$ ). Analysis of the donor and acceptor natural transition orbitals<sup>29</sup> suggests that the  $\pi$  orbitals for the two pyridine ligands are orthogonal to one another,

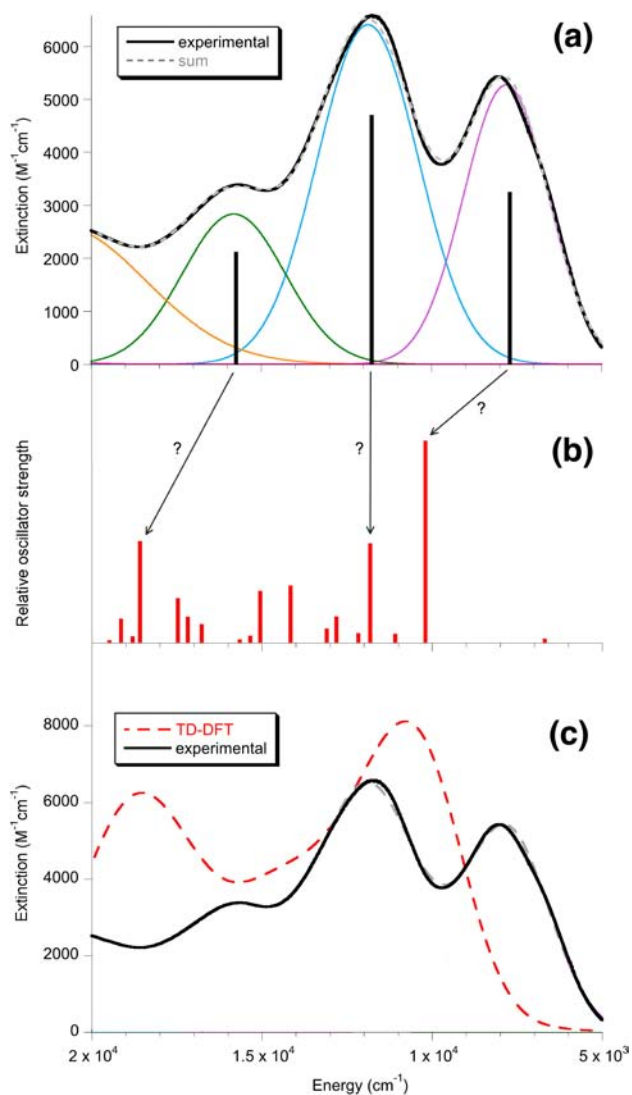


**Figure 10.** (a) Gaussian fit to the electronic absorption spectrum. The experimental spectrum is a thick black line; individual Gaussians are thin colored lines, and the sum of the fit Gaussians is a dashed gray line. (b) Calculated transitions, and a tentative correlation with observed bands (arrows). (c) Experimental spectrum and Gaussian fits from the spectrum in panel a, overlaid upon a predicted spectrum (dashed red line) based on the calculated transitions.

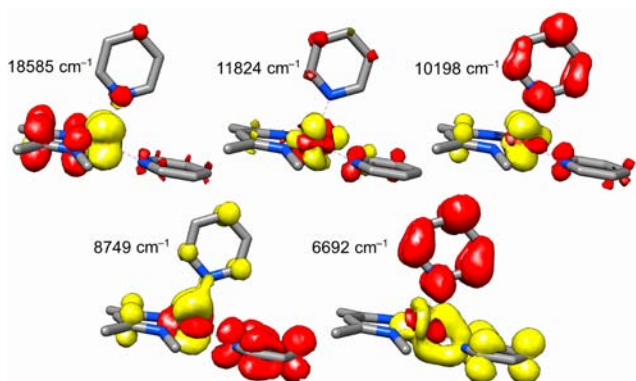


**Figure 11.** Electron density difference maps for key predicted transitions. Electrons move from yellow areas to red areas upon excitation.

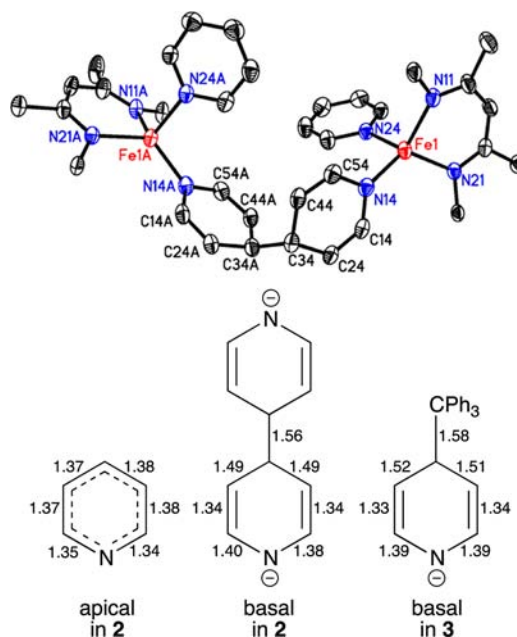


**Figure 12.** (top) Molecular structure of  $\{L^{\text{Me}}\text{FePy}\}_2(\mu\text{-C}_{10}\text{H}_{10}\text{N}_2)$  (**2**), using 50% thermal ellipsoids. The cocrystallized solvent, 2,6-diisopropylphenyl groups, and hydrogen atoms have been removed for clarity. Selected bond distances (Å): C34–C34A, 1.563(6); Fe1–N14, 1.942(3); Fe1–N24, 2.123(3); Fe1–N11, 1.999(3); Fe1–N21, 2.003(3). (Bottom) Bond lengths (Å) in the apical pyridine ligand of **2**, the basal (coupled) pyridines of **2**, and the basal (coupled) pyridine of **3** (see below). Uncertainties in the crystallographically determined bond distances are less than 0.01 Å.

which offers a reasonable explanation why the LLCT transitions have small oscillator strengths. Thus, the excited-state computations suggest that the LLCT transition often cited as evidence for a ligand radical<sup>3,18</sup> can be very small and that intense low-energy bands should be assigned with care in these complexes.

**Coupling of Unprotected Pyridine Ligands Forms a New C–C Bond in a Diiron(II) Complex.** Addition of 2 equiv of pyridine (Py) to  $L^{\text{Me}}\text{Fe}(\eta^6\text{-benzene})$  or 4 equiv of Py to  $L^{\text{Me}}\text{FeNNFe}L^{\text{Me}}$  in pentane results in an immediate color change to green. Crystallization from the concentrated *green* solutions gives *red* crystals in 92% yield. The molecular structure of  $\{L^{\text{Me}}\text{FePy}\}_2(\mu\text{-C}_{10}\text{H}_{10}\text{N}_2)$  (**2**) shows that pyridine ligands from different iron centers couple to form a C–C bond between the *para* positions of each ring (Figure 12). We presume that this C–C coupling did not occur in **1** because of the bulky *tert*-butyl substituents.

In the crystal structure of **2**, the diiron molecule lies on a crystallographic 2-fold rotation axis that bisects the central C–C bond; thus one-half of the molecule is unique. Reduction of the pyridine to give a bridging dianionic ligand is consistent with electron localization as C–C double bonds in the heterocycle (Figure 12, bottom). The bond lengths of C14–C24 (1.336(5) Å) and C44–C54 (1.339(5) Å) indicate C–C double bonds, while the bond lengths of C24–C34 (1.494(5) Å) and C34–C44 (1.488(5) Å) indicate C–C single bonds. The C–N bond lengths for C14–N14 and C54–N14, 1.383(4) Å and 1.397(4) Å, are closer to C–N single bonds. The C34–C34A bond, which links the two rings, is a C–C single bond (1.563(6) Å). The presence of the unusual

dianionic bridging ligand implies an oxidation state of +2 at both iron atoms.

The effective magnetic moment of solid **2** above 200 K is about  $7.0 \mu_B$ , which is slightly higher than the spin-only value for two uncoupled high-spin iron(II) ions ( $6.3 \mu_B$ ). The presence of weak ferromagnetic coupling is shown by a slight increase of the values at lower temperatures with a maximum at about 15 K (Figure S6, Supporting Information). The data could be simulated with an exchange coupling constant  $J = +0.6 \text{ cm}^{-1}$ ,  $g_{av} = 2.01$ , and moderately strong zero-field splitting of  $D = +13 \text{ cm}^{-1}$ .

The zero-field Mössbauer spectrum of solid **2** at 80 K has a symmetric quadrupole doublet with  $\delta = 0.77 \text{ mm/s}$  and  $|\Delta E_Q| = 1.57 \text{ mm/s}$  (Figure 8, bottom). The isomer shift is again within the range of four-coordinate high-spin iron(II)  $\beta$ -diketiminato complexes ( $\delta = 0.69\text{--}0.90 \text{ mm/s}$  and  $|\Delta E_Q| = 1.32\text{--}3.12 \text{ mm/s}$ ).<sup>20,22,30</sup> The isomer shift of **2** is close to the isomer shift of **1** ( $\delta = 0.79 \text{ mm/s}$ ), consistent with the similar Fe–N(diketiminato) and Fe–N(basal pyridine) bond lengths in the crystal structures of **1** and **2**.<sup>31</sup> The similarity between **1** and **2** in the isomer shift and in the distances between iron and the key in-plane ligands are consistent with the idea that the iron remains in the same oxidation state. The iron(II) formulation will also be discussed below in the context of compound **3**.

**In Solution, **2** Dissociates To Give Monomeric  $L^{Me}Fe(Py)_2$  (**2**<sub>1</sub>).** Dissolving the red crystals of **2** in pentane, toluene, Et<sub>2</sub>O, or THF gives a green solution, suggesting a change in the structure of the complex. The solution absorption spectrum of **2** is strikingly similar to the absorption spectrum of **1** (Figure 13). This includes the intense absorption bands in

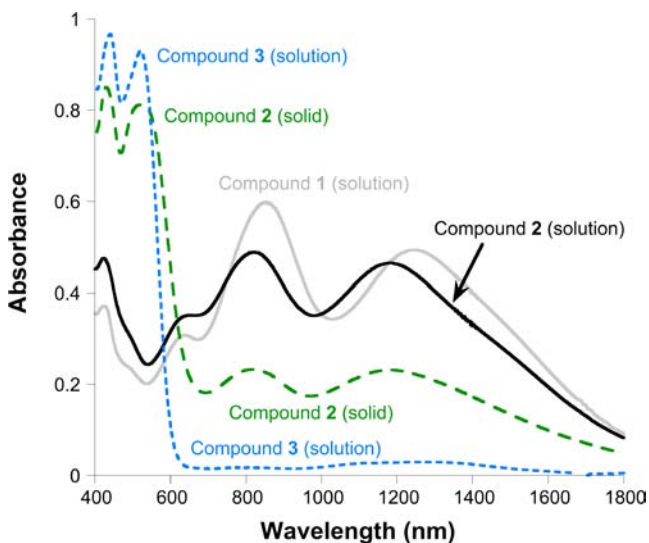


**Figure 13.** Electronic absorption spectra of  $\{L^{Me}FePy\}_2(\mu-C_{10}H_{10}N_2)$  (**2**) as a solution (solid black line) and as a solid (dashed green line), compared with the spectrum of  $L^{Me}Fe(t^BuPy)_2$  (**1**) in hexane (gray line) and of  $L^{Me}Fe(Py)(NC_5H_5CPh_3)$  (**3**) in toluene (blue dashed line).

the long-wavelength region, which in **2** are slightly blue-shifted to  $\lambda_{max} = 820 \text{ nm}$  ( $\epsilon = 5600 \text{ M}^{-1} \text{ cm}^{-1}$ ) and  $1185 \text{ nm}$  ( $\epsilon = 5300 \text{ M}^{-1} \text{ cm}^{-1}$ ). The similarity of the electronic absorption spectrum of **2** in solution to that of **1** suggests that dissolved **2** is in the form  $L^{Me}Fe(Py)_2$  (**2**<sub>1</sub>).

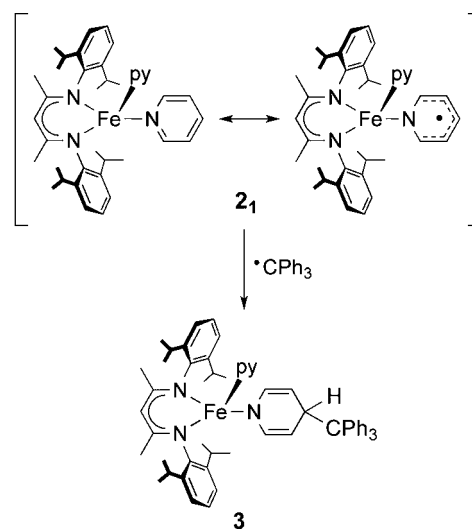
Comparison of the solution and solid-state electronic absorption spectra of **2** (Figure 13) indicates a significant difference in electronic structure. The spectrum in the solid state (formed by drying a thin film on a glass slide) has maxima at  $\lambda_{max} = 430$  and  $522 \text{ nm}$ . These agree well with those for compound **3**, which has a reduced pyridine ligand as in **2** (see below). Smaller peaks at longer wavelength align with **2**<sub>1</sub>, indicating that dimerization is not complete under these conditions.

Compound **2** has  $C_2$  symmetry in the solid state, but the <sup>1</sup>H NMR spectrum of **2** in  $C_6D_6$  has relatively few peaks, suggesting higher solution symmetry as might occur if **2** were dissociating into monomeric units. The addition of pyridine (10 equiv) does not change the spectrum. The resonances could not be assigned fully, due to overlaps with solvent resonances, but the small number of peaks is clearly inconsistent with the low-symmetry solid-state structure. Importantly, the diketiminato peaks that could be assigned by relative integrations have chemical shifts close to the analogous peaks in the <sup>1</sup>H NMR spectrum of **1**. Thus, <sup>1</sup>H NMR spectroscopy also supports the production of monomeric  $L^{Me}Fe(Py)_2$  (**2**<sub>1</sub>) in solution.

The derivative X-band EPR spectrum of a frozen solution of **2** in toluene at 6 K (Figure S7, Supporting Information) closely resembles the spectrum of **1**. The observation of an EPR signal in perpendicular mode ( $B_1 \perp B_0$ ) suggests a half-integer spin system, which is inconsistent with the diiron(II) formulation indicated by solid-state crystallographic and Mössbauer data. Attempts to collect clean Mössbauer spectra of solutions of **2** have been unsuccessful. However, the EPR and UV–vis evidence serve as very strong evidence that **2** has a structure in solution (**2**<sub>1</sub>) that resembles **1**.

As an additional test of the solution structure and radical pyridine character on **2**<sub>1</sub>, a solution of **2** was treated with triphenylmethyl radical ( $\cdot CPh_3$ , which is isolated as the “Gomberg dimer”<sup>32</sup>). Adding 1 equiv of  $\cdot CPh_3$  per iron in **2** gave an immediate change to a red compound (**3**, Scheme 1) with a visible spectrum that closely resembles the solid-state spectrum of **2** (Figure 13). X-ray crystallography revealed that the structure of **3** (Figure 14) has a new C–C bond akin to that in the solid-state form of **2**. The new C–C bond in **3** (C34–C64 =  $1.575(6) \text{ \AA}$ ) is the same length as the C–C bond in the

**Scheme 1.** Reactivity of **2**<sub>1</sub> with Triphenylmethyl Radical To Form **3**



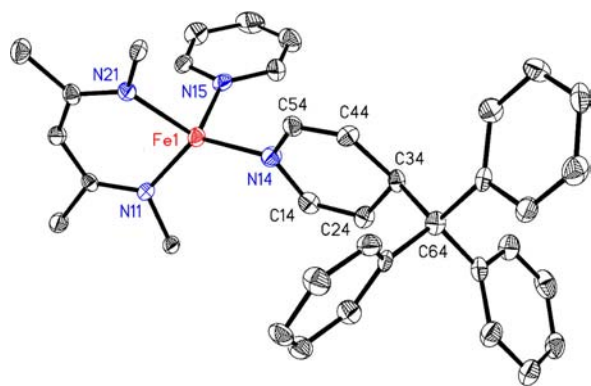


**Figure 14.** Molecular structure of  $L^{\text{Me}}\text{Fe}(\text{Py})(\text{NC}_5\text{H}_5\text{CPh}_3)$  (**3**), using 50% thermal ellipsoids. The 2,6-diisopropylphenyl groups and hydrogen atoms have been removed for clarity. Selected bond distances (Å): Fe1–N11, 1.992(3); Fe1–N21, 1.999(3); Fe1–N14, 1.945(4); Fe1–N15, 2.119(4); C34–C64, 1.575(6). See Figure 12 for bond distances within the pyridine ring.

dimer **2** (1.563(6) Å). By comparison, the coupling of two triphenylmethyl radicals (Gomberg's dimer) yields a relatively long C–C bond (1.597(4) Å).<sup>33</sup> In addition, the C–C and C–N bond lengths of the reduced pyridine ligands in compounds **2** and **3** are very similar, as shown in Figure 12.

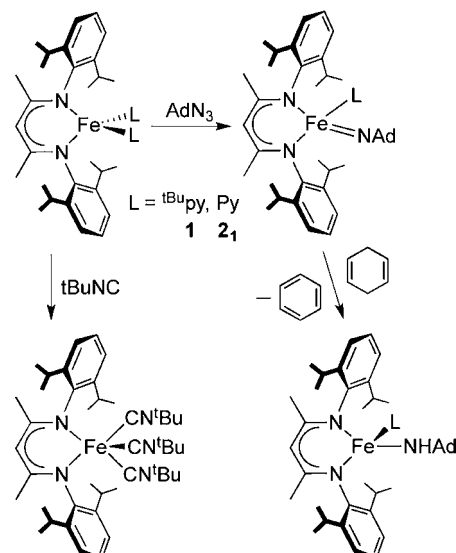
Other spectroscopic parameters of **3** are very similar to those for **2**. Its visible spectrum ( $\lambda_{\text{max}} = 438/519$  vs 430/522) and Mössbauer spectrum ( $\delta = 0.75$  vs 0.77 mm/s,  $|\Delta E_{\text{Q}}| = 1.66$  vs 1.57 mm/s) are almost identical to those of solid-state **2**. The isomer shifts ( $\delta$ ) are similar to those of  $\beta$ -diketiminato iron(II) complexes bearing two nitrogen ligands with anionic character,  $\{L^{\text{Me}}\text{Fe}\}_2(\text{N}_6\text{Ad}_2)$  ( $\delta = 0.75$ )<sup>22</sup> and  $\text{K}[L^{\text{Me}}\text{Fe}(\text{AdNNNNAd})]$  ( $\delta = 0.81$ ).<sup>20</sup> These data, as well as solution magnetic measurements, are consistent with **2** and **3** having high-spin iron(II) electronic configurations. Also, the coupling of  $^{\bullet}\text{CPh}_3$  with **2**<sub>1</sub> to give **3**, an iron(II) product with a reduced ligand and a new C–C bond, serves as additional support for radical character at the *para* position of the pyridine ring in **2**<sub>1</sub>.

**Complexes 1 and 2 Have the Same Solution Reactivity.** If the iron(II) complex  $\{L^{\text{Me}}\text{FePy}\}_2(\mu\text{-C}_{10}\text{H}_{10}\text{N}_2)$  (**2**) is present as the monomeric complex  $L^{\text{Me}}\text{Fe}(\text{Py})_2$  (**2**<sub>1</sub>) in solution, it should react like **1** in reactions that do not involve the pyridine ligand directly. Since **1** is expected to act as a source of the “ $L^{\text{Me}}\text{Fe}$ ” fragment through displacement of the pyridine ligands, we tested **1** and **2** in previously established reactions of  $\beta$ -diketiminato-supported iron(I) precursors, as shown in Scheme 2.

In previous work,  $L^{\text{Me}}\text{FeNNFeL}^{\text{Me}}$  was shown to react with pyridines and adamantyl azide ( $\text{N}_3\text{Ad}$ ) to give a short-lived four-coordinate iron(III) imido complex,  $L^{\text{Me}}\text{Fe}(\text{Py})(\text{NAd})$ .<sup>34,35</sup> Imido complexes with various *para*-substituted pyridines react rapidly with weak C–H bonds to give the well-characterized four-coordinate iron(II) amido complex,  $L^{\text{Me}}\text{Fe}(\text{Py})(\text{NHAd})$ .<sup>35</sup> The addition of 1 equiv of  $\text{N}_3\text{Ad}$  and 10 equiv of 1,4-cyclohexadiene to **1** in  $\text{C}_6\text{D}_6$  yields the previously characterized<sup>34,35</sup> amido complex  $L^{\text{Me}}\text{Fe}(\text{t}^{\text{Bu}}\text{py})(\text{NHAd})$  in 91% yield based on an internal  $^1\text{H}$  NMR integration standard (Scheme 2). Exposure of compound **2** to the same reaction conditions gives the analogous amido complex  $L^{\text{Me}}\text{Fe}(\text{Py})(\text{NHAd})$  in 68% yield.

Also,  $L^{\text{Me}}\text{FeNNFeL}^{\text{Me}}$  is known to react quantitatively with *tert*-butylisocyanide ( $\text{CN}^{\text{tBu}}$ ) to give the iron(I) tris(isocyanide) complex,  $L^{\text{Me}}\text{Fe}(\text{CN}^{\text{tBu}})_3$  (Scheme 2).<sup>36</sup>  $L^{\text{Me}}\text{Fe}$

**Scheme 2.** Reactivity of **1** and **2**<sub>1</sub>



$(\text{CN}^{\text{tBu}})_3$  is a low-spin ( $S = 1/2$ ) iron(I) compound that can be easily identified and quantified by double integration of its derivative X-band EPR spectrum at 77 K. Addition of  $\sim 10$  equivalents of  $\text{CN}^{\text{tBu}}$  to a solution of **1** in toluene yields a solution of  $L^{\text{Me}}\text{Fe}(\text{CN}^{\text{tBu}})_3$  in quantitative yield. Likewise, the exposure of a solution of **2** in toluene to  $\sim 10$  equiv of  $\text{CN}^{\text{tBu}}$  yields  $L^{\text{Me}}\text{Fe}(\text{CN}^{\text{tBu}})_3$  in 81% yield based on an EPR integration standard. Since **2** reacts as iron(I) in solution, it either must be present in solution as  $L^{\text{Me}}\text{Fe}(\text{py})_2$  (**2**<sub>1</sub>) or can easily be converted to this form.

Overall, the reactivity of **2** is consistent with the hypothesis that **2** uncouples in solution to produce **2**<sub>1</sub>, which behaves similarly to **1**. Despite the iron(II) character in the ground state of these complexes, they react in a way that indicates that the metal maintains the reducing ability of an iron(I) complex.

## DISCUSSION

**Ligand Redox Noninnocence in  $L^{\text{Me}}\text{Fe}(\text{t}^{\text{Bu}}\text{py})_2$ .** Magnetic, EPR, and computational data show that  $L^{\text{Me}}\text{Fe}(\text{t}^{\text{Bu}}\text{py})_2$  (**1**) has an  $S = 3/2$  ground state. This implies that **1** is formally high-spin iron(I). However, a reducible ligand such as pyridine can accept charge to give a ground state in which one electron from the iron center is transferred to the ligand. The result is a high-spin iron(II) complex ( $S_{\text{Fe}} = 2$ ) and a coordinated radical anion ( $S_{\text{L}} = 1/2$ ) that are antiferromagnetically coupled to give a  $S_{\text{total}} = 3/2$  ground state. As long as the antiferromagnetic coupling is sufficiently strong, this situation cannot be distinguished from the high-spin iron(I) form on the basis of the bulk magnetism or the EPR data alone.

The presence of redox-active ligands in metal complexes makes the determination of the metal oxidation state ambiguous without extensive experimental evidence using a combination of quantum chemical calculations and spectroscopic techniques.<sup>1,4</sup> Mössbauer spectroscopy (in particular the isomer shift) has been used in a number of cases to establish the “physical” oxidation state of an iron ion.<sup>37</sup> However, high-spin iron(I) and high-spin iron(II) centers have similar isomer shifts, which complicates assignment of the oxidation state in **1**.

It is important to recall that a filled iron *d* orbital can also *backbond* into an empty  $\pi^*$  orbital on the  $\text{t}^{\text{Bu}}\text{py}$  ligand. This is partial donation of an *electron pair* from iron to pyridine, which

is not the same as donation of a single electron (as in redox noninnocence) because the spin density on the ligand is the same sign as the metal in backbonding but has the opposite sign as the metal in a radical ligand complex with antiferromagnetic coupling between the metal and ligand.<sup>38</sup> Formally iron(I) complexes supported by bulky  $\beta$ -diketiminate ligands have been shown to exhibit both of these bonding scenarios (one-electron transfer and two-electron backbonding).<sup>21</sup> For example,  $L^{\text{Me}}\text{FeNNFe}L^{\text{Me}}$  has a overall spin of  $S = 3$  and is formally diiron(I).<sup>14</sup> However, experimental and computational studies concluded that  $L^{\text{Me}}\text{FeNNFe}L^{\text{Me}}$  is best described as two high-spin iron(II) centers ( $S = 2$ ) that are antiferromagnetically coupled to a reduced dinitrogen ligand with a spin of  $S = 1$ .<sup>39</sup> In contrast, the formally iron(I) complex  $L^{\text{Me}}\text{Fe}(\text{t}^{\text{Bu}}\text{CN})_2$  has only two-electron backbonding, based on experimental and computational data.<sup>21</sup> In these examples, examination of the experimental and computational results together was necessary to clarify the electronic structure of the complex.

In this context, we evaluate the data for **1**. The bond distances from the iron to the basal pyridine in the X-ray crystal structure are significantly shorter than expected for a  $\text{t}^{\text{Bu}}\text{py}$  ligand with a dative bond to iron. Most strikingly, the distance to the basal pyridine nitrogen is the shortest Fe–N<sub>py</sub> distance in the literature.<sup>16</sup> In addition, the C–N bond lengths within the basal  $\text{t}^{\text{Bu}}\text{py}$  ligand are elongated by 0.03–0.04 Å relative to free pyridine, which also indicates extra electron density on the  $\text{t}^{\text{Bu}}\text{py}$  ligand. These effects are consistent with either  $\pi$ -backbonding or reduction of the basal  $\text{t}^{\text{Bu}}\text{py}$  ligand.

The quantum-chemical model of the quartet state of **1** shows one  $\beta$  electron in an orbital that can be described as the bonding combination of the  $d_z^2$  orbital with the  $\pi^*$  orbital on the basal  $\text{t}^{\text{Bu}}\text{py}$  ligand. This bonding interaction causes the short Fe–N<sub>py</sub> bond distance discussed above. The overlap ( $S$ ) of the orbitals containing the corresponding  $\alpha$  and  $\beta$  electrons is 0.89.<sup>40</sup> This value is not as low as in many well-characterized ligand-radical complexes, which are often in the 0.3–0.5 range and unambiguously indicate a radical ligand with antiferromagnetic coupling to the metal.<sup>41</sup> Values in the range of 0.7–0.9 indicate that the antiferromagnetic coupling between the ligand and the metal is increasingly large but are still indicative of ligand radicals.<sup>42</sup> In **1**, the exchange coupling is calculated as ca.  $-1200\text{ cm}^{-1}$ ,<sup>43</sup> and this strong antiferromagnetic coupling prevents any significant thermal population of states above the quartet ground state.

Importantly, the spin density on the basal pyridine in **1** is opposite of that on the metal, which is a clear sign of a significant contribution from a resonance structure with high-spin iron(II) complex and a coordinated radical (Figure 4, right). Also indicating radical character, the unprotected compound **2** reacts with  $\cdot\text{CPh}_3$  at the pyridine ligand to give a radical coupling product (**3**). On the other hand, the DFT results indicate that the pyridines do not accept a full electron in the ground state: the highest-lying  $\beta$  electron lies largely on the metal as well as the pyridine ligand, and the high-intensity electronic absorption bands at low energy have primarily MLCT character rather than LLCT character, indicating significant contribution from an iron(I) resonance structure. Therefore, we describe **1** and **2**, as being a resonance hybrid between these two structures.

**$\{L^{\text{Me}}\text{FePy}\}_2(\mu\text{-C}_{10}\text{H}_{10}\text{N}_2)$  (**2**) Is Formed by the Coupling of Pyridine Ligand Radicals.** In the pinacol coupling reaction, one-electron reduction of a ketone or aldehyde yields carbon radicals that couple to form a pinacol product.<sup>44</sup> We

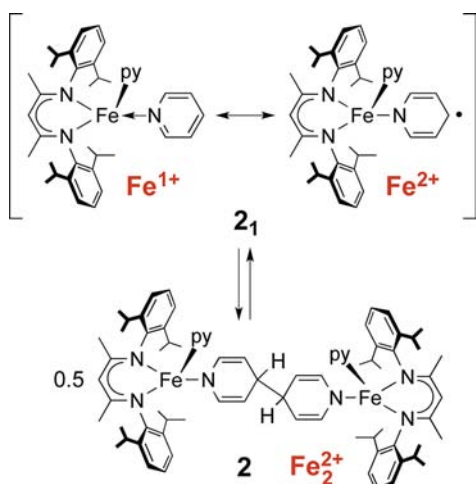
have reported the coupling of acetophenone by  $L^{\text{Me}}\text{FeNNFe}L^{\text{Me}}$  to give the corresponding diiron(II) pinacolate complex, which was suggested to come from one-electron reduction of the ketone.<sup>14</sup> However, in that case, there was no spectroscopic evidence for an intermediate with a bound radical.

As noted in the Introduction, pyridine can be reduced electrochemically or with strong chemical reducing agents. The pyridine radical anion itself dimerizes to give a coupled dimeric dianion, on a time scale of seconds to minutes.<sup>45</sup> In liquid ammonia, CV data suggest that the coupling reaction is reversible.<sup>7</sup> The spectroscopic and structural methods available in transition-metal complexes can lead to better characterization of this phenomenon. It should be noted that there are examples of irreversible coupling of pyridine via reduction with strong alkali<sup>39</sup> and main group<sup>46</sup> reducing agents. There are also main-group compounds where radical pyridine groups have been identified<sup>41</sup> and an interesting reduced iron–pyridinediimine complex in which the *para* position of the pyridine formed a new bond to another iron atom.<sup>47</sup>

The reductive coupling of pyridine ligands by transition metals to give the reduced dianion is rare.<sup>11,12</sup> Literature examples of the reductive coupling of pyridine by d-block (Sc, Ti)<sup>12</sup> and f-block (Sm, Tm)<sup>13</sup> metals to give the corresponding metal complex use highly reducing metal centers and yield a diamido ligand like that observed here. There are also other examples where the reductive coupling of pyridine results in the formation of bipyridine from a subsequent oxidation that occurs in the reaction conditions.<sup>11</sup> All of these examples are stoichiometric; however, the catalytic dehydrogenative coupling of pyridines to give bipy was recently reported.<sup>48</sup> To our knowledge, compound **2** is the first report of the reductive coupling of pyridine with iron, and it is the only example with any metal where the coupling is reversible. A related reversible coupling reaction of imidazole ligands was reported recently.<sup>49</sup>

The crystal structure of **2** shows C–C and C–N bond distances that are consistent with localized electrons in the bridging ligand, and a long C–C single bond between the halves of the ligand. Solid state magnetic susceptibility and Mössbauer data are consistent with **2** being a diiron(II) complex. However, dissolution of dark red crystals of **2** in organic solvents yielded a dark green solution with <sup>1</sup>H NMR, electronic absorption, and EPR spectroscopic properties similar to **1**. These spectroscopic measurements are complemented by reactivity studies showing a close analogy between the reaction products from **1** and from **2** in solution. These results show that the reductive coupling of **2** is reversible to give monomeric  $L^{\text{Me}}\text{Fe}(\text{py})_2$  (**2**<sub>1</sub>) in solution (Scheme 3).

The low barrier and the reversibility of the radical dimerization in Scheme 3 are surprising. Reversible reductive coupling of ligand C–C bonds can be spontaneous<sup>6,49</sup> but typically requires addition of a reagent.<sup>50</sup> In a different example, reduction of a cationic molybdenum diazotolyl complex yielded a C–C bond via radical dimerization of the diazotolyl ligands on different metals, which was reversed upon the addition of cobaltocene.<sup>50b</sup> The behavior of **2** is reminiscent of Gomberg's dimer of triphenylmethyl radicals, which rapidly interconverts between monomeric and dimeric forms.<sup>32</sup> In Gomberg's dimer, the bond dissociation enthalpy has been measured as  $\Delta H = 11\text{ kcal/mol}$ .<sup>51</sup> Although it has not been possible to measure the equilibrium constant between **2**<sub>1</sub> and **2** because of the inability to analyze sufficiently concentrated solutions, the bond energy

Scheme 3. Reversible Interconversion of **2** and **2**<sub>1</sub> through Radical Coupling

of the new C–C bond in **2** must be similar (roughly 10 kcal/mol).

In the system described here, it is exciting that the electrons stored in the C–C bond can be used to produce an incipient iron(I) center that does further chemistry. For example, dissolving **2** and adding 1-adamantyl azide (AdN<sub>3</sub>) gives the iron(III) imido complex L<sup>Me</sup>Fe(NAd)(Py), which in turn can activate C–H bonds. This is related to other recent work using redox-active ligand complexes,<sup>1,4,52</sup> but differs in that the potentially unstable ligand radical is “protected” by formation of a C–C bond. This type of reversible dimerization is not limited to the reductive chemistry used here; reversible formation of a C–N bond was recently described in a highly oxidizing iron(III)–imido radical complex.<sup>53</sup>

The observations in this paper raise a more general question: how much ground-state ligand radical character is needed to observe radical reactions at the ligand? This general question cannot be answered thoroughly from the single example studied here in depth, but it is clear that the ligand radical character in **1** is less than that in many other ligand radical complexes.<sup>1–3</sup> We speculate that the C–C bond formation in this system is reversible *because* the radical character on the pyridine is limited; a more developed radical would be higher in energy and tip the thermodynamic balance toward the formation of the C–C bond.

## CONCLUSIONS

Pyridines coordinate to diketiminate-supported iron(I) to give bis(pyridine) adducts in solution. Spectroscopic studies show that the compounds have an  $S = 3/2$  ground state. Spectroscopically calibrated DFT calculations and bond lengths show that the basal pyridine has significant radical character. Thus, the ground state is balanced between iron(I) and high-spin iron(II) antiferromagnetically coupled to a radical. Unless protected with a *tert*-butyl group, the *para* positions on the basal pyridines can form new C–C bonds. Reaction with triphenylmethyl radical leads to a complex with an amido ligand derived from the pyridines, and the *para* positions can also couple to form a bimetallic complex with a bridging diamido ligand. The dimerized product is formally diiron(II), because the reducing electrons are fully transferred to the bridging ligand. Surprisingly, the dimerization is rapidly reversible, and

thus the electrons stored in the C–C bond can be used to achieve iron(I)-like reactivity from an iron(II) complex.

## EXPERIMENTAL SECTION

**General Considerations.** All manipulations were performed under an argon atmosphere (or nitrogen atmosphere where specified) by Schlenk techniques or in an M. Braun glovebox maintained at or below 1 ppm of O<sub>2</sub> and H<sub>2</sub>O. Glassware was dried at 150 °C overnight, and Celite was dried overnight at 200 °C under vacuum. Pentane, hexane, benzene, diethyl ether, and toluene were purified by passage through activated alumina and Q5 columns from Glass Contour Co. THF was distilled under N<sub>2</sub> from a potassium benzophenone ketyl solution. All solvents were degassed prior to entry into the argon glovebox. All solvents were stored over 3 Å molecular sieves. Benzene-*d*<sub>6</sub> was dried and stored over flame-activated alumina. Toluene-*d*<sub>8</sub> and THF-*d*<sub>8</sub> were vacuum transferred from sodium benzophenone ketyl solutions and were stored over 3 Å molecular sieves. Before use, an aliquot of each solvent was tested with a drop of sodium benzophenone ketyl in THF solution. Pyridine and 4-*tert*-butylpyridine were dried by either distillation or vacuum transfer from calcium hydride and were stored over 3 Å molecular sieves. 1-Adamantyl azide was crystallized from pentane prior to use, and *tert*-butylisocyanide was used as received. L<sup>Me</sup>FeNNFeL<sup>Me</sup> and L<sup>Me</sup>Fe( $\eta^6$ -benzene) were prepared by published procedures.<sup>14</sup> Gombert’s dimer (1-diphenylmethylene-4-triphenylmethyl-2,5-cyclohexadiene) was prepared according to a published procedure.<sup>54</sup>

<sup>1</sup>H NMR data were recorded on a Bruker Avance 500 spectrometer (500 MHz) or a Bruker Avance 400 spectrometer (400 MHz). All resonances in the <sup>1</sup>H NMR spectra are referenced to residual protonated solvents: benzene ( $\delta$  7.16 ppm), toluene ( $\delta$  2.09 ppm), or THF ( $\delta$  3.58 or 1.73 ppm). Resonances were singlets unless otherwise noted. X-band EPR spectra were recorded on a Bruker EMXplus spectrometer with a perpendicular-mode cavity. An Oxford Instruments ESR 900 cryostat and Oxford Instruments ITC503 temperature controller were used to maintain the set temperature. IR data were recorded on a Shimadzu FTIR spectrophotometer (FTIR-8400S) using a KBr pellet. UV–vis spectra were recorded on a Cary 50 spectrophotometer using Schlenk-adapted quartz cuvettes with a 1 mm optical path length. NIR spectra were recorded on a Perkin-Elmer Lambda 950 UV–vis–NIR spectrometer using Schlenk-adapted quartz cuvettes with a 1 mm optical path length. Solid state vis–NIR spectra were recorded on a Perkin-Elmer Lambda 950 UV–vis–NIR spectrometer by drying a thin film of solution on a glass plate, which was inserted into a 1 cm optical path length cuvette. Solution magnetic susceptibilities were determined by the Evans method.<sup>55</sup> Elemental analyses were obtained from the CENTC Elemental Analysis Facility at the University of Rochester. Microanalysis samples were weighed with a PerkinElmer model AD-6 autobalance, and their compositions were determined with a PerkinElmer 2400 series II analyzer and handled in a VAC Atmospheres glovebox under argon.

**Synthesis of L<sup>Me</sup>Fe(*t*BuPy)<sub>2</sub> (**1**).** L<sup>Me</sup>Fe( $\eta^6$ -benzene) (246 mg, 0.446 mmol) was dissolved in pentane (10 mL) to produce a red-orange solution. 4-*tert*-Butylpyridine (132.5  $\mu$ L, 0.905 mmol) was added to the solution, which resulted in an immediate color change to green. The solution was stirred for 2 h and then filtered through Celite, concentrated to 1 mL, and stored at –45 °C for 2 d. This yielded 219 mg of semicrystalline green product. The mother liquor was concentrated to 0.5 mL and was cooled to –45 °C to give a second crop of product (54 mg). The total yield was 273 mg (82.2%). L<sup>Me</sup>FeNNFeL<sup>Me</sup> can also be used instead of the benzene complex to give the desired product with a comparable yield. <sup>1</sup>H NMR (C<sub>6</sub>D<sub>6</sub>, 25 °C):  $\delta$  23.4 (4H), 10.1 (4H), 6.3 (2H, aryl *p*-H), 3.6 (18H, <sup>*t*</sup>Bu <sup>*1*</sup>Bu), 2.0 (4H), –4.3 (br, 12H + 12H, <sup>*i*</sup>Pr CH<sub>3</sub>), –30.4 (4H), –82.9 (1H,  $\alpha$ -H), –136.0 (6H, backbone CH<sub>3</sub>) ppm. The resonances that integrate for 4H can be assigned as <sup>*i*</sup>Pr-CH, aryl *m*-H, <sup>*t*</sup>Bu <sup>*o*</sup>-H, or <sup>*t*</sup>Bu <sup>*m*</sup>-H.  $\mu_{\text{eff}}$  (C<sub>6</sub>D<sub>6</sub>, 25 °C) 3.7(1)  $\mu_{\text{B}}$ . IR (KBr): 3064 (m), 3022 (w), 2961 (s), 2923 (s), 2902 (s), 2865 (s), 2491 (m), 2437 (w), 1597 (w), 1569 (vs), 1508 (m), 1491 (m), 1460 (m), 1430 (m), 1396 (s), 1359 (m), 1315 (s), 1273 (m), 1260 (m), 1227 (w), 1217 (w), 1192 (vs), 1174

(m), 1123 (w), 1099 (w), 1057 (w), 1022 (w), 1006 (w), 964 (vs), 933 (m), 837 (m), 821 (m), 793 (w), 758 (m), 714 (m)  $\text{cm}^{-1}$ . UV–vis (hexane): 320 (18  $\text{mM}^{-1} \text{cm}^{-1}$ ), 424 (3.9  $\text{mM}^{-1} \text{cm}^{-1}$ ), 490 (sh, 2  $\text{mM}^{-1} \text{cm}^{-1}$ ), 636 (3.3  $\text{mM}^{-1} \text{cm}^{-1}$ ), 847 (6.4  $\text{mM}^{-1} \text{cm}^{-1}$ ), 1245 (5.6  $\text{mM}^{-1} \text{cm}^{-1}$ ) nm. Anal. Calcd for  $\text{C}_{47}\text{H}_{67}\text{N}_4\text{Fe}$ : C, 75.88; H, 9.10; N, 7.53. Found: C, 76.10; H, 9.72; N, 7.59.

**Synthesis of  $[\text{L}^{\text{Me}}\text{Fe}(\text{Py})]_2(\mu\text{-C}_{10}\text{H}_{10}\text{N}_2)$  (2).**  $\text{L}^{\text{Me}}\text{FeNNFeL}^{\text{Me}}$  (200 mg, 0.205 mmol) was dissolved in THF (12 mL) to give a purple solution. Pyridine (84  $\mu\text{L}$ , 1.0 mmol) was added to the solution, which resulted in an immediate color change to green. The solution was stirred for 3 h and was filtered through Celite. The green solution was concentrated to 2 mL and was layered with pentane (12 mL) and allowed to stand at room temperature. This produced 167 mg of crystalline red solid. A second crop of product was obtained by concentrating the mother liquor to 2 mL and layering with additional pentane (8 mL). The solution was cooled to  $-45^\circ\text{C}$ , which yielded 85 mg of red solid product. The total yield was 252 mg (92.0%). Characterization of solid  $[\text{L}^{\text{Me}}\text{FePy}]_2(\mu\text{-C}_{10}\text{H}_{10}\text{N}_2)$ . IR (KBr): 3055 (m), 3017 (m), 2961 (s), 2924 (s), 2866 (s), 2789 (w), 2751 (w), 2507 (w), 1642 (s), 1555 (s), 1513 (s), 1460 (s), 1434 (s), 1390 (vs), 1316 (vs), 1281 (m), 1261 (m), 1230 (w), 1209 (w), 1182 (vs), 1150 (w), 1110 (m), 1057 (w), 1021 (w), 985 (s), 934 (vs), 848 (w), 793 (m), 781 (w), 758 (s), 716 (m), 701 (m)  $\text{cm}^{-1}$ . Solid state vis (thin film):  $\lambda_{\text{max}}$  434, 526, 808 nm. Anal. Calcd for  $\text{C}_{78}\text{H}_{102}\text{N}_8\text{Fe}_2\text{C}_4\text{H}_8\text{O}$ : C, 73.74; H, 8.31; N, 8.39. Found: C, 73.97; H, 8.35; N, 8.34. Solution characterization of  $\text{L}^{\text{Me}}\text{Fe}(\text{Py})_2$  (2<sub>1</sub>) from solid  $[\text{L}^{\text{Me}}\text{FePy}]_2(\mu\text{-C}_{10}\text{H}_{10}\text{N}_2)$  (as discussed in the text).  $^1\text{H}$  NMR ( $\text{C}_6\text{D}_6$ ,  $25^\circ\text{C}$ ):  $\delta$  22.8 (4H), 10.1, 3.4 (12H,  $^i\text{Pr}$   $\text{CH}_3$ ), 2.0,  $-4.2$  (br, 12H,  $^i\text{Pr}$   $\text{CH}_3$ ),  $-30.4$  (2H, aryl *p*-H or py *p*-H),  $-120$  (6H, backbone  $\text{CH}_3$ ) ppm. Some overlapping resonances prevented reliable integration, and small amounts of THF and pentane were visible in the spectrum.  $\mu_{\text{eff}}$  ( $\text{C}_6\text{D}_6$ ,  $26^\circ\text{C}$ ) 4.1(1)  $\mu_{\text{B}}$ . UV–vis (toluene): 325 (17  $\text{mM}^{-1} \text{cm}^{-1}$ ), 423 (4.5  $\text{mM}^{-1} \text{cm}^{-1}$ ), 500 (br sh, 3  $\text{mM}^{-1} \text{cm}^{-1}$ ), 630 (sh, 4  $\text{mM}^{-1} \text{cm}^{-1}$ ), 820 (5.6  $\text{mM}^{-1} \text{cm}^{-1}$ ), 1185 (5.3  $\text{mM}^{-1} \text{cm}^{-1}$ ) nm.

**Synthesis of  $\text{L}^{\text{Me}}\text{Fe}(\text{Py})(\text{NC}_5\text{H}_5\text{CPh}_3)$  (3).**  $\text{L}^{\text{Me}}\text{FeNNFeL}^{\text{Me}}$  (200 mg, 0.205 mmol) was dissolved in THF (10 mL) to give a purple solution. Pyridine (83  $\mu\text{L}$ , 1.0 mmol) was added to the solution, and the reaction mixture was stirred for 2.5 h. Gomberg's dimer ( $\text{Ph}_6\text{C}_2\cdot$ /2hexane, 115 mg, 0.216 mmol) was dissolved in THF (3 mL) and transferred to the green reaction mixture, which resulted in an immediate color change to red. After the mixture was stirred for 1 h, the solvent was removed under reduced pressure. Pentane (1 mL) was added, and the solvent was again removed under reduced pressure to yield a red solid. The residue was extracted with toluene (12 mL) and filtered through Celite, and the resulting red solution was concentrated to 10 mL. Vapor diffusion of pentane into the toluene solution yielded 170 mg (47%) of 3 as red crystals.  $^1\text{H}$  NMR ( $\text{C}_6\text{D}_6$ ,  $25^\circ\text{C}$ ):  $\delta$  58.9, 50.4, 34.8, 29.4, 23.9, 21.3, 13.0, 9.1,  $-0.8$ ,  $-9.2$ ,  $-10.4$ ,  $-12.9$ ,  $-38.4$ ,  $-42.3$ ,  $-55.9$ ,  $-79.5$ ,  $-84.2$ ,  $-97.9$  ppm. Overlap of peaks prevented accurate integration of the resonances.  $\mu_{\text{eff}}$  ( $\text{C}_6\text{D}_6$ ,  $25^\circ\text{C}$ ) 4.9(1)  $\mu_{\text{B}}$ . IR (KBr): 3055 (w), 3026 (w), 2961 (s), 2926 (m), 2866 (w), 1641 (m), 1597 (w), 1568 (w), 1514 (m), 1495 (m), 1462 (m), 1437 (s), 1387 (vs), 1315 (s), 1290 (w), 1261 (m), 1231 (w), 1175 (m), 1105 (w), 1030 (m), 1003 (s), 934 (w), 795 (m), 750 (m), 733 (m), 702 (s)  $\text{cm}^{-1}$ . UV–vis (toluene): 331 (19  $\text{mM}^{-1} \text{cm}^{-1}$ ), 440 (3.8  $\text{mM}^{-1} \text{cm}^{-1}$ ), 521 (3.6  $\text{mM}^{-1} \text{cm}^{-1}$ ) nm. Anal. Calcd for  $\text{C}_{38}\text{H}_{66}\text{N}_4\text{Fe}$ : C, 79.61; H, 7.60; N, 6.40. Found: C, 79.53; H, 7.53; N, 6.30.

**Mössbauer Spectroscopy.** Mössbauer data were recorded on a spectrometer with alternating constant acceleration. The minimum experimental line width was 0.24 mm/s (full width at half-height). The sample temperature was maintained constant in an Oxford Instruments Variox cryostat. The  $\gamma$ -source was  $^{57}\text{Co}/\text{Rh}$ . Isomer shifts are quoted relative to iron metal at 300 K. The zero-field spectra were simulated as Lorentzian doublets.

**Magnetic Susceptibility Measurements.** Magnetic susceptibility data were measured from powder samples of solid material in the temperature range 2–300 K by using a SQUID susceptometer (MPMS-7, Quantum Design) with a field of 1.0 T. The experimental data were corrected for underlying diamagnetism by use of tabulated Pascal's constants. The susceptibility data,  $\chi T(T)$  or  $\mu_{\text{eff}}(T)$ , were

simulated with the julX package for exchange coupled systems written by E.B. The simulations are based on either the usual spin-Hamilton operator for a symmetric dinuclear complex with two spin  $S_i = 2$  (eq 1) or the usual spin-Hamilton operator for mononuclear complexes with spin  $S = 3/2$  (eq 2), where  $g$  is the average electronic  $g$  value, and  $D$  and  $E/D$  are the axial zero-field splitting and rhombicity parameters for the iron sites. The magnetic moments were obtained from the first-order derivative of the eigenvalues of the Hamiltonian operator shown above. Powder summations were done by using a 16-point Lebedev grid.

$$\hat{H} = -2J\hat{S}_1 \cdot \hat{S}_2 + g\beta(\hat{S}_1 + \hat{S}_2) \cdot \vec{B} + \sum_{i=1,2} D[\hat{S}_{i,z}^2 - 1/3S(S+1) + E/D(\hat{S}_{i,x}^2 - \hat{S}_{i,y}^2)] \quad (1)$$

$$\hat{H} = g\mu_{\text{B}}\hat{S} \cdot \vec{B} + D[\hat{S}_z^2 - 1/3S(S+1) + E/D(\hat{S}_x^2 - \hat{S}_y^2)] \quad (2)$$

**Computational Details.** The calculations were performed using ORCA version 2.8.<sup>56</sup> Single point calculations at the crystallographic structure with the TPSSH functional<sup>23</sup> were used to analyze the electronic structure and accelerated with the RIJCOSX approximation.<sup>57</sup> The TZVP basis set was used for Fe, N, and C, and the SVP basis set for H.<sup>58</sup> Scalar relativistic corrections were introduced according to the ZORA approximation.<sup>59</sup> We tested different initial guesses for the electronic structure including the quartet and the broken-symmetry (4,1) state, and all converged to the solution given here.

The isomer shift ( $\delta$ ) is related to the  $s$  electron density at the nucleus and can be calculated using the formula

$$\delta = \alpha(\rho_0 - C) + \beta \quad (3)$$

where  $\rho_0$  is the electron density at the nucleus and the constants  $\alpha$ ,  $\beta$ , and  $C$  are from a linear regression analysis to literature compounds.<sup>25</sup> The quadrupole splitting depends on the electric field gradient at the iron nucleus and is calculated by the formula

$$\Delta E_Q = \frac{1}{2}eQV_{zz}\left(1 + \frac{\eta^2}{3}\right)^{1/2} \quad (4)$$

where  $e$  is the electric charge of an electron,  $Q$  is the nuclear quadrupole moment of Fe, and  $V_{xx}$ ,  $V_{yy}$ , and  $V_{zz}$  are components of the electric field gradient tensor.  $\eta$  is the asymmetry parameter,  $\eta = (|V_{xx} - V_{yy}|/|V_{zz}|)$ , chosen such that  $|V_{zz}| \geq |V_{yy}| \geq |V_{xx}|$ .

In the TD-DFT calculations 20 roots were determined. The compositions of the calculated excitations are given in the Supporting Information. Orbital plots were created using Chimera version 1.6.<sup>60</sup> The spectral simulation and fitting used the orca\_asa module.<sup>61</sup>

**X-ray Crystallography.** Crystals were placed on the tip of a 0.1 mm diameter glass capillary tube or fiber and mounted on a Bruker SMART APEX II diffractometer<sup>62</sup> for data collection at 100.0(1) K using Mo  $K\alpha$  radiation and a graphite monochromator. A randomly oriented region of reciprocal space was surveyed: six groups of frames were collected with  $0.50^\circ$  steps in  $\omega$  at six different  $\varphi$  settings and a detector position of  $-38^\circ$  in  $2\theta$ . The intensity data were corrected for absorption.<sup>63</sup> Final cell constants were calculated from the  $xyz$  centroids of >3750 strong reflections from the actual data collection after integration.<sup>64</sup> The structures were solved using SIR97<sup>65</sup> and refined using SHELXL-97.<sup>66</sup> The space groups were determined based on systematic absences and intensity statistics. Direct-methods solutions were calculated, which provided most non-hydrogen atoms from the E-map. Full-matrix least-squares/difference Fourier cycles located the remaining non-hydrogen atoms. All non-hydrogen atoms were refined with anisotropic displacement parameters. All hydrogen atoms were placed in idealized positions and refined as riding atoms with relative isotropic displacement parameters. Details of the crystal structures are presented in Table 1.

For 1, the refinement stalled at  $R1 = 0.179$ , indicating that twin and solvent modeling were required. The nonmerohedral twin law was

Table 1. Details of X-ray Crystal Structures

compd	$L^{Me}Fe(tBuPy)_2$ (1)	$\{L^{Me}Fe(Py)\}_2(\mu-C_{10}H_{10}N_2)$ (2)	$L^{Me}Fe(py)$ ( $NC_5H_5CPh_3$ ) (3)
empirical formula	$C_{47}H_{67}N_4Fe$	$C_{83}H_{114}N_8Fe_2$	$C_{38}H_{66}N_4Fe$
FW	743.90	1335.52	874.99
cryst syst	triclinic	orthorhombic	monoclinic
space group	$P\bar{1}$	$Pnna$	$P2_1/n$
<i>a</i> (Å)	14.552(4)	14.676(3)	14.783(2)
<i>b</i> (Å)	17.226(5)	34.656(8)	17.156(3)
<i>c</i> (Å)	22.142(6)	14.788(3)	18.848(3)
$\alpha$ (deg)	87.924(5)	90	90
$\beta$ (deg)	73.640(5)	90	92.150(3)
$\gamma$ (deg)	77.200(5)	90	90
<i>V</i> (Å <sup>3</sup> )	5191(2)	7521(3)	4776.8(13)
<i>Z</i>	4	4	4
$\rho$ (g/cm <sup>3</sup> )	0.952	1.179	1.217
$\mu$ (mm <sup>-1</sup> )	0.320	0.434	0.358
<i>R</i> <sub>1</sub> , <i>wR</i> <sub>2</sub> ( <i>I</i> > 2 $\sigma$ ( <i>I</i> ))	0.0946, 0.2333	0.0649, 0.1244	0.0666, 0.1239
<i>R</i> <sub>1</sub> , <i>wR</i> <sub>2</sub> (all data)	0.1718, 0.2683	0.1099, 0.1417	0.1425, 0.1513
GOF	0.940	1.064	1.013

determined as  $[-1\ 0\ 0/0\ -1\ 0/-0.876\ 0.071\ 1]$ , a 180° rotation about reciprocal lattice  $[0\ 0\ 1]$ .<sup>67</sup> The data were reintegrated, and a new absorption correction was applied.<sup>63</sup> There were 9894 unique reflections associated solely with one component, 9867 unique reflections associated solely with the second component, and 25929 unique overlapping reflections. The mass ratio of the two components refined to 69:31.

In 1, there are two independent iron molecules, with all atoms in general positions, and two independent solvent sites in the asymmetric unit. One solvent area, which spanned a crystallographic inversion center, was not modeled satisfactorily. The two-component data from the integration were transformed to “de-twinned” one-component data with TWINABS,<sup>68</sup> which removed the contributions to the structure factors from the second (minor) component. The one-component data were modified by PLATON, function SQUEEZE,<sup>69</sup> which subtracted the contributions of the disordered solvent from the structure factors; 474 electrons in 1265 Å<sup>3</sup> per unit cell were removed in total. The final full-matrix least-squares refinement converged to *R*<sub>1</sub> = 0.0946 (*F*<sup>2</sup>, *I* > 2 $\sigma$ (*I*)) and *wR*<sub>2</sub> = 0.2683 (*F*<sup>2</sup>, all data).

For 2, the di-iron molecule lies on a crystallographic 2-fold axis that bisects the bond between atoms C34 and C34A; thus one-half of the molecule is unique. There is also a cocrystallized pentane solvent molecule, which was modeled as disordered over a crystallographic 2-fold axis (50:50). The final full matrix least-squares refinement converged to *R*<sub>1</sub> = 0.0649 (*F*<sup>2</sup>, *I* > 2 $\sigma$ (*I*)) and *wR*<sub>2</sub> = 0.1417 (*F*<sup>2</sup>, all data).

For 3, the final full matrix least-squares refinement converged to *R*<sub>1</sub> = 0.0666 (*F*<sup>2</sup>, *I* > 2 $\sigma$ (*I*)) and *wR*<sub>2</sub> = 0.1513 (*F*<sup>2</sup>, all data).

## ■ ASSOCIATED CONTENT

### ● Supporting Information

Additional spectra, computational details, and crystallographic details in CIF format. This material is available free of charge via the Internet at <http://pubs.acs.org>.

## ■ AUTHOR INFORMATION

### Corresponding Author

[holland@chem.rochester.edu](mailto:holland@chem.rochester.edu)

### Notes

The authors declare no competing financial interest.

## ■ ACKNOWLEDGMENTS

This work was supported by the National Science Foundation (Grant CHE-0911314 to P.L.H.), by a Fulbright Award (P.L.H.), and by the Max-Planck-Gesellschaft (F.N.).

## ■ REFERENCES

- (1) (a) Kaim, W. *Coord. Chem. Rev.* **1987**, *76*, 187. (b) Pierpont, C. G. *Coord. Chem. Rev.* **2001**, *216–217*, 99. (c) de Bruin, B.; Hetterscheid, D. G. H.; Koekkoek, A. J. J.; Grützmacher, H. *Prog. Inorg. Chem.* **2007**, *55*, 247. (d) Chirik, P. J.; Wieghardt, K. *Science* **2010**, *327*, 794. (e) Chirik, P. J. *Inorg. Chem.* **2011**, *50*, 9737. (f) Kaim, W. *Inorg. Chem.* **2011**, *50*, 9752. (g) Kaim, W. *Eur. J. Inorg. Chem.* **2012**, *343*. (h) van der Vlugt, J. I. *Eur. J. Inorg. Chem.* **2012**, *363*. (i) Lyaskovkyy, V.; de Bruin, B. *ACS Catal.* **2012**, *2*, 270.
- (2) (a) Reedijk, J. *Heterocyclic Nitrogen-donor Ligands. In Comprehensive Coordination Chemistry: The Synthesis, Reactions, Properties and Applications of Coordination Compounds*; Wilkinson, G., Gillard, R. D., McCleverty, J. A., Eds.; Pergamon Press: Oxford, U.K., 1987; Vol. 2, Chapter 13.2. (b) Constable, E. C. *Adv. Inorg. Chem.* **1989**, *34*, 1. (c) Braterman, P. S.; Song, J.-I.; Peacock, R. D. *Inorg. Chem.* **1992**, *31*, 555. (d) Creutz, C. *Comments Inorg. Chem.* **1982**, *1*, 293. (e) Irwin, M.; Jenkins, R. K.; Denning, M. S.; Krämer, T.; Grandjean, F.; Long, G. J.; Herchel, R.; McGrady, J. E.; Goicoechea, J. M. *Inorg. Chem.* **2010**, *49*, 6160.
- (3) (a) Juris, A.; Balzani, V.; Barigelletti, F.; Campagna, S.; Belser, P.; von Zelewsky, A. *Coord. Chem. Rev.* **1988**, *84*, 85. (b) Evans, W. J.; Drummond, D. K. *J. Am. Chem. Soc.* **1989**, *111*, 3329. (c) Ramos Sende, J. A.; Arana, C. R.; Hernández, K. T.; Keshevarz-K., M.; Abruña, H. D. *Inorg. Chem.* **1995**, *34*, 9773. (d) Fedushkin, I. L.; Petrovskaya, T. V.; Girgsdies, F.; Köhn, R. D.; Bochkarev, M. N.; Schumann, H. *Angew. Chem., Int. Ed.* **1999**, *38*, 2262. (e) Schultz, M.; Boncella, J. M.; Berg, D. J.; Tilley, T. D.; Andersen, R. A. *Organometallics* **2002**, *21*, 460. (f) Scarborough, C. C.; Wieghardt, K. *Inorg. Chem.* **2011**, *50*, 9773 and references therein.
- (4) Examples: (a) Bart, S. C.; Chlopek, K.; Bill, E.; Bouwkamp, M. W.; Lobkovsky, E.; Neese, F.; Wieghardt, K.; Chirik, P. J. *J. Am. Chem. Soc.* **2006**, *128*, 13901. (b) Lu, C. C.; Bill, E.; Weyhermüller, T.; Bothe, E.; Wieghardt, K. *J. Am. Chem. Soc.* **2008**, *130*, 3181. (c) Wile, B. M.; Trovitch, R. J.; Bart, S. C.; Tondreau, A. M.; Lobkovsky, E.; Milsman, C.; Bill, E.; Wieghardt, K.; Chirik, P. J. *Inorg. Chem.* **2009**, *48*, 4190. (d) Bowman, A. C.; Milsman, C.; Hojilla Atienza, C. C.; Lobkovsky, E.; Wieghardt, K.; Chirik, P. J. *J. Am. Chem. Soc.* **2010**, *132*, 1676. (e) Bowman, A. C.; Milsman, C.; Bill, E.; Lobkovsky, E.; Weyhermüller, T.; Wieghardt, K.; Chirik, P. J. *Inorg. Chem.* **2010**, *49*, 6110. (f) Joy, S.; Krämer, T.; Paul, N. D.; Banerjee, P.; McGrady, J. E.; Goswami, S. *Inorg. Chem.* **2011**, *50*, 9993.
- (5) (a) Bachman, J.; Nocera, D. G. *J. Am. Chem. Soc.* **2004**, *126*, 2829. (b) Bachman, J.; Nocera, D. G. *Inorg. Chem.* **2005**, *44*, 6930. (c) Bachman, J.; Nocera, D. G. *J. Am. Chem. Soc.* **2005**, *127*, 4730. (d) Bachmann, J.; Hodgkiss, J. M.; Young, E. R.; Nocera, D. G. *Inorg. Chem.* **2007**, *46*, 607.
- (6) (a) Frazier, B. A.; Wolczanski, P. T.; Lobkovsky, E. B.; Cundari, T. R. *J. Am. Chem. Soc.* **2009**, *131*, 3428. (b) Frazier, B. A.; Wolczanski, P. T.; Keresztes, I.; DeBeer, S.; Lobkovsky, E. B.; Pierpont, A. W.; Cundari, T. R. *Inorg. Chem.* **2012**, *51*, 8177.
- (7) Meites, L.; Zuman, P. *CRC Handbook Series in Organic Electrochemistry*, Vol. 1; CRC Press: Cleveland, 1977.
- (8) (a) Kaim, W. *Inorg. Chem.* **1984**, *23*, 504. (b) Gross, C.; Kaim, W. *Angew. Chem., Int. Ed.* **1985**, *24*, 856.
- (9) (a) Setifi, F.; Ouahab, L.; Golhen, S.; Yoshida, Y.; Saito, G. *Inorg. Chem.* **2003**, *42*, 1791. (b) Pointillart, F.; Maury, O.; Le Gal, Y.; Golhen, S.; Cador, O.; Ouahab, L. *Inorg. Chem.* **2009**, *48*, 7421.
- (10) Selected examples: (a) Grumbine, S. D.; Chadha, R. K.; Tilley, T. D. *J. Am. Chem. Soc.* **1992**, *114*, 1518. (b) Duplessis, E. A.; Jelliss, P. A.; Kirkpatrick, C. C.; Minter, S. D.; Wampler, K. M. *J. Organomet. Chem.* **2006**, *691*, 4660. (c) Cohen, B. W.; Polyansky, D. E.; Zong, R.; Zhou, H.; Ouk, T.; Cabelli, D. E.; Thummel, R. P.; Fujita, E. *Inorg. Chem.* **2010**, *49*, 8034.

- (11) (a) Cockerton, B. R.; Deeming, A. J. *J. Organomet. Chem.* **1992**, *426*, C36. (b) Deelman, B.-J.; Stevels, W. M.; Teuben, J. H.; Lakin, M. T.; Spek, A. L. *Organometallics* **1994**, *13*, 3881. (c) Duval, P. B.; Burns, C. J.; Clark, D. L.; Morris, D. E.; Scott, B. L.; Thompson, J. D.; Werkema, E. L.; Jia, L.; Andersen, R. A. *Angew. Chem., Int. Ed.* **2001**, *40*, 3357. (d) Sen Soo, H.; Diaconescu, P. L.; Cummins, C. C. *Organometallics* **2004**, *23*, 498. (e) Carver, C. T.; Diaconescu, P. L. *J. Am. Chem. Soc.* **2008**, *130*, 7558.
- (12) (a) Durfee, L. D.; Fanwick, P. E.; Rothwell, I. P.; Foltz, K.; Huffman, J. C. *J. Am. Chem. Soc.* **1987**, *109*, 4720. (b) Huang, W.; Khan, S. I.; Diaconescu, P. L. *J. Am. Chem. Soc.* **2011**, *133*, 10410.
- (13) (a) Jaroschik, F.; Nief, F.; Le Goff, X.-F.; Ricard, L. *Organometallics* **2007**, *26*, 3552. (b) Fedushkin, I. L.; Nevodchikov, V. I.; Bochkarev, M. N.; Dechert, S.; Schumann, H. *Russ. Chem. Bull., Int. Ed.* **2003**, *52*, 154. (c) Labouille, S.; Nief, F.; Le Goff, X.-F.; Maron, L.; Kindra, D. R.; Houghton, H. L.; Ziller, J. W.; Evans, W. J. *Organometallics* **2012**, *31*, 5196.
- (14) Smith, J. M.; Sadique, A. R.; Cundari, T. R.; Rodgers, K. R.; Lukat-Rodgers, G.; Lachicotte, R. J.; Flaschenriem, C. J.; Vela, J.; Holland, P. L. *J. Am. Chem. Soc.* **2006**, *128*, 756.
- (15) The complex Fe(NO)(py)(NR<sub>2</sub>)<sub>2</sub> could be viewed as iron(I), depending on the formalism used for oxidation states. Stokes, S. L.; Davis, W. M.; Odom, A. L.; Cummins, C. C. *Organometallics* **1996**, *15*, 4521.
- (16) Cambridge Structural Database, v. 5.32 (Aug 2011 update). Allen, F. H. *Acta Crystallogr.* **2002**, *B58*, 380–388.
- (17) The average Fe–N<sub>py</sub> bond distance of 2.15 ± 0.08 Å was calculated from 903 Fe–pyridine compounds in the Cambridge Structural Database. The minimum distance in the database is 1.965(9) Å. See: Balch, A. L.; Noll, B. C.; Olmstead, M. M.; Phillips, S. L. *Inorg. Chem.* **1996**, *35*, 6495.
- (18) (a) König, E.; Kremer, S. *Chem. Phys. Lett.* **1970**, *5*, 87. (b) Heath, G. A.; Yellowlees, L. J.; Braterman, P. S. *J. Chem. Soc., Chem. Commun.* **1981**, 287. (c) Heath, G. A.; Yellowlees, L. J.; Braterman, P. S. *Chem. Phys. Lett.* **1982**, *92*, 646. (d) Khusniyarov, M. M.; Weyhermüller, T.; Bill, E.; Wieghardt, K. *J. Am. Chem. Soc.* **2009**, *131*, 1208. (e) Scarborough, C. C.; Lancaster, K. M.; DeBeer, S.; Weyhermüller, T.; Sproules, S.; Wieghardt, K. *Inorg. Chem.* **2012**, *51*, 3718.
- (19) The short-lived nature of the radical anion of pyridine has prevented experimental measurement of its electronic absorption spectrum. TD-DFT computations on the unligated pyridine radical anion predict a  $\pi$ - $\pi^*$  band at 1224 nm but with a very weak intensity.
- (20) Cowley, R. E.; Bill, E.; Neese, F.; Brennessel, W. W.; Holland, P. L. *Inorg. Chem.* **2009**, *48*, 4828.
- (21) Cowley, R. E.; Christian, G. J.; Brennessel, W. W.; Neese, F.; Holland, P. L. *Eur. J. Inorg. Chem.* **2012**, 479.
- (22) Cowley, R. E.; Elhaik, J.; Eckert, N. A.; Brennessel, W. W.; Bill, E.; Holland, P. L. *J. Am. Chem. Soc.* **2008**, *130*, 6074.
- (23) Jensen, K. P. *Inorg. Chem.* **2008**, *47*, 10357. This functional has been shown to be effective for predicting Mössbauer isomer shifts: see ref 25.
- (24) Neese, F. ORCA – an ab initio, Density Functional and Semiempirical Program Package, version 2.9, 2012.
- (25) The DFT calculations give the electron density at the iron nucleus, which correlates with the isomer shift (standard deviation of the correlation for a training set of literature compounds was ~ 0.1 mm/s). Römel, M.; Ye, S.; Neese, F. *Inorg. Chem.* **2009**, *48*, 784.
- (26) The same solution was reached whether or not the quartet was input as the broken-symmetry BS(4,1) starting point.
- (27) The agreement between TD-DFT results and observed spectra is variable. For details, see: (a) Neese, F. *J. Biol. Inorg. Chem.* **2006**, *11*, 702. (b) Neese, F. *Coord. Chem. Rev.* **2009**, *253*, 526.
- (28) The intensity of this band is surprising for one based on  $d-d$  transitions; further study will explore this phenomenon in more detail.
- (29) Batista, E. R.; Martin, R. L. *Natural Transition Orbitals. Encyclopedia of Computational Chemistry*; Wiley: New York, 2004.
- (30) Vela, J.; Stoian, S.; Flaschenriem, C. J.; Münck, E.; Holland, P. L. *J. Am. Chem. Soc.* **2004**, *126*, 4522.
- (31) The isomer shift correlates well with changes in metal–ligand distances. See: Neese, F.; Petrenko, T. In *Mössbauer Spectroscopy and Transition Metal Chemistry*; Gülich, P., Bill, E., Trautwein, A. X., Eds.; Springer: Berlin, 2011; p 137.
- (32) (a) Williams, D. J.; Kreilick, R. J. *Am. Chem. Soc.* **1967**, *89*, 3408. (b) Forrester, A. R.; Hay, J. M.; Thomson, R. H. *Organic Chemistry of Stable Free Radicals*; Academic Press: London, 1968. (c) Abakumov, G. A.; Cherkasov, V. K.; Nevodchikov, V. I.; Druzhkov, N. O.; Fukin, G. K.; Kursky, Y. A.; Piskunov, A. V. *Tetrahedron Lett.* **2005**, *46*, 4095. (d) *Stable Radicals: Fundamentals and Applied Aspects of Odd-Electron Compounds*; Hicks, R. G., Ed.; Wiley: Chichester, U.K., 2010.
- (33) Bochkarev, L. N.; Molosnova, N. E.; Zakharov, L. N.; Fukin, G. K.; Yanovsky, A. I.; Struchkov, Y. T. *Acta Crystallogr.* **1995**, *CS1*, 489.
- (34) Eckert, N. A.; Vaddadi, S.; Stoian, S.; Lachicotte, R. J.; Cundari, T. R.; Holland, P. L. *Angew. Chem., Int. Ed.* **2006**, *45*, 6868.
- (35) Cowley, R. E.; Eckert, N. A.; Vaddadi, S.; Figg, T. M.; Cundari, T. R.; Holland, P. L. *J. Am. Chem. Soc.* **2011**, *133*, 9796.
- (36) Cowley, R. E.; Eckert, N. A.; Elhaik, J.; Holland, P. L. *Chem. Commun.* **2009**, 1760.
- (37) Selected references: (a) Ray, K.; Bill, E.; Weyhermüller, T.; Wieghardt, K. *J. Am. Chem. Soc.* **2005**, *127*, 5641. (b) Ghosh, P.; Bill, E.; Weyhermüller, T.; Wieghardt, K. *J. Am. Chem. Soc.* **2003**, *125*, 3967. (c) Patra, A. K.; Bill, E.; Weyhermüller, T.; Stobie, K.; Bell, Z.; Ward, M. D.; McCleverty, J. A.; Wieghardt, K. *Inorg. Chem.* **2006**, *45*, 6541. (d) Chlopek, K.; Bill, E.; Weyhermüller, T.; Wieghardt, K. *Inorg. Chem.* **2005**, *44*, 7087. (e) Ghosh, P.; Begum, A.; Bill, E.; Weyhermüller, T.; Wieghardt, K. *Inorg. Chem.* **2003**, *42*, 3208.
- (38) Chirik, P. J. *Inorg. Chem.* **2011**, *50*, 9737.
- (39) Stoian, S. A.; Vela, J.; Smith, J. M.; Sadique, A. R.; Holland, P. L.; Münck, E.; Bominaar, E. L. *J. Am. Chem. Soc.* **2006**, *128*, 10181.
- (40) A detailed description of the use of the overlap from broken-symmetry calculations is given in: (a) Herebian, D.; Bothe, E.; Neese, F.; Weyhermüller, T.; Wieghardt, K. *J. Am. Chem. Soc.* **2003**, *125*, 9116. (b) Neese, F. *J. Phys. Chem. Solids* **2004**, *65*, 781.
- (41) Examples: (a) Blanchard, S.; Neese, F.; Bothe, E.; Bill, E.; Weyhermüller, T.; Wieghardt, K. *Inorg. Chem.* **2005**, *44*, 3636. (b) Chlopek, K.; Bothe, E.; Neese, F.; Weyhermüller, T.; Wieghardt, K. *Inorg. Chem.* **2006**, *45*, 6298.
- (42) (a) Patra, A. K.; Bill, E.; Bothe, E.; Chlopek, K.; Neese, F.; Weyhermüller, T.; Stobie, K.; Ward, M. D.; McCleverty, J. A.; Wieghardt, K. *Inorg. Chem.* **2006**, *45*, 7877. (b) Surawatanawong, P.; Sproules, S.; Neese, F.; Wieghardt, K. *Inorg. Chem.* **2011**, *50*, 12064. (c) Tomson, N. C.; Crimmin, M. R.; Petrenko, T.; Rosebrugh, L. E.; Sproules, S.; Boyd, W. C.; Bergman, R. G.; DeBeer, S.; Toste, F. D.; Wieghardt, K. *J. Am. Chem. Soc.* **2011**, *133*, 18785. (d) Stieber, S. C. E.; Milsmann, C.; Hoyt, J. M.; Turner, Z. R.; Finkelstein, K. D.; Wieghardt, K.; DeBeer, S.; Chirik, P. J. *Inorg. Chem.* **2012**, *51*, 3770.
- (43) (a) Yamaguchi, K.; Takahara, Y.; Fueno, T. In *Applied Quantum Chemistry* Smith, V. H., Ed.; Ridel: Dordrecht, The Netherlands, 1986; p 155. (b) Soda, T.; Kitagawa, Y.; Onishi, T.; Takano, Y.; Shigeta, Y.; Nagao, H.; Yoshioka, Y.; Yamaguchi, K. *Chem. Phys. Lett.* **2000**, *319*, 223.
- (44) Smith, M. B.; March, J. *March's Advanced Organic Chemistry*, 5th ed.; Wiley: New York, 2001.
- (45) (a) Talcott, C. L.; Meyers, R. J. *Mol. Phys.* **1967**, *12*, 549. (b) Chaudhuri, J.; Kume, S.; Jagur-Grodzinski, J.; Szwarc, M. *J. Am. Chem. Soc.* **1968**, *90*, 6421. (c) Buick, A. R.; Kemp, T. J.; Neal, G. T.; Stone, T. J. *J. Chem. Soc. A* **1969**, 1609. (d) Schmulbach, C. D.; Hinckley, C. C.; Wasmund, D. *J. Am. Chem. Soc.* **1968**, *90*, 6600. (e) Kalyanaraman, V.; Rao, C. N. R.; George, M. V. *J. Chem. Soc. B* **1971**, 2406. (f) Fessenden, R. W.; Neta, P. *Chem. Phys. Lett.* **1973**, *18*, 14. (g) Rainis, A.; Szwarc, M. *J. Phys. Chem.* **1975**, *79*, 106. (h) Olah, G. A.; Hunadi, R. *J. Org. Chem.* **1981**, *46*, 715.
- (46) (a) Bychkov, V. T.; Vyazankin, N. S.; Cherepennikova, N. F.; Razuvaev, G. A. *Zh. Obshch. Khim.* **1973**, *43*, 629. (b) Mitchell, T. N. *J. Chem. Soc., Perkin Trans. 2* **1976**, 1149. (c) Ziegler, E.; Fuchs, G.; Lehmkuhl, H. *Z. Anorg. Allg. Chem.* **1967**, *355*, 145. (d) Kynast, U.; Skelton, B. W.; White, A. H.; Henderson, M. J.; Raston, C. L. *J. Organomet. Chem.* **1990**, *384*, C1.

- (47) Scott, J.; Vidyaratne, I.; Korobkov, I.; Gambarotta, S.; Budzelaar, P. H. M. *Inorg. Chem.* **2008**, *47*, 896.
- (48) Kawashima, T.; Takao, T.; Suzuki, H. *J. Am. Chem. Soc.* **2007**, *129*, 11006.
- (49) Monreal, M. J.; Diaconescu, P. L. *J. Am. Chem. Soc.* **2010**, *132*, 7676.
- (50) (a) Venkatesan, K.; Blacque, O.; Fox, T.; Alfonso, M.; Schmalle, H. W.; Berke, H. *Organometallics* **2004**, *23*, 1183. (b) Curley, J. J.; Murahashi, T.; Cummins, C. C. *Inorg. Chem.* **2009**, *48*, 7181. (c) Boni, A.; Funaioli, T.; Marchetti, F.; Pampaloni, G.; Pinzino, C.; Zacchini, S. *Organometallics* **2011**, *30*, 4115.
- (51) (a) Ziegler, K.; Ditzel, F. *Justus Liebig's Ann. Chem.* **1929**, 473, 194. (b) Colle, T. H.; Glaspie, P. S.; Lewis, E. S. *J. Org. Chem.* **1978**, *43*, 2722. (c) Neumann, W. P.; Uzick, W.; Zarkadis, A. K. *J. Am. Chem. Soc.* **1986**, *108*, 3762.
- (52) (a) Haneline, M. R.; Heyduk, A. F. *J. Am. Chem. Soc.* **2006**, *128*, 8410. (b) Ketterer, N. A.; Fan, H.; Blackmore, K. J.; Yang, X.; Ziller, J. W.; Baik, M.-H.; Heyduk, A. F. *J. Am. Chem. Soc.* **2008**, *130*, 4364. (c) Blackmore, K. J.; Ziller, J. W.; Heyduk, A. F. *Inorg. Chem.* **2005**, *44*, 5559. (d) Blackmore, K. J.; Sly, M. B.; Haneline, M. R.; Ziller, J. W.; Heyduk, A. F. *Inorg. Chem.* **2008**, *47*, 10522. (e) Smith, A. L.; Hardcastle, K. I.; Soper, J. D. *J. Am. Chem. Soc.* **2010**, *132*, 14358.
- (53) King, E. R.; Hennessy, E. T.; Betley, T. A. *J. Am. Chem. Soc.* **2011**, *133*, 4917.
- (54) Ghosh, P.; Fagan, P. J.; Marshall, W. J.; Hauptman, E.; Bullock, R. M. *Inorg. Chem.* **2009**, *48*, 6490–6500.
- (55) (a) Baker, M. V.; Field, L. D.; Hambley, T. W. *Inorg. Chem.* **1988**, *27*, 2872. (b) Schubert, E. M. *J. Chem. Educ.* **1992**, *69*, 62.
- (56) Neese, F. ORCA 2.8; Universität Bonn, Bonn, Germany, 2011.
- (57) (a) Neese, F.; Wennmohs, F.; Hansen, A.; Becker, U. *Chem. Phys.* **2009**, *356*, 98–109. (b) Kossmann, S.; Neese, F. *Chem. Phys. Lett.* **2009**, *481*, 240–43.
- (58) Pantazis, D. A.; Chen, X. Y.; Landis, C. R.; Neese, F. *J. Chem. Theory Comput.* **2008**, *4*, 908.
- (59) (a) van Lenthe, E.; Baerends, E. J.; Snijders, J. G. *J. Chem. Phys.* **1993**, *99*, 4597. (b) van Lenthe, E.; Baerends, E. J.; Snijders, J. G. *J. Chem. Phys.* **1994**, *101*, 9783. (c) van Lenthe, E.; van Leeuwen, R.; Baerends, E. J.; Snijders, J. G. *Int. J. Quantum Chem.* **1996**, *57*, 281.
- (60) Pettersen, E. F.; Goddard, T. D.; Huang, C. C.; Couch, G. S.; Greenblatt, D. M.; Meng, E. C.; Ferrin, T. E. *J. Comput. Chem.* **2004**, *25*, 1605.
- (61) Petrenko, T.; Neese, F. *J. Chem. Phys.* **2007**, *127*, No. 164319.
- (62) APEX2, version 2010.7-0; Bruker AXS: Madison, WI, 2010.
- (63) Sheldrick, G. M. SADABS, version 2008/1; University of Göttingen: Göttingen, Germany, 2008.
- (64) SAINT, version 7.68A; Bruker AXS: Madison, WI, 2009.
- (65) Altomare, A.; Burla, M. C.; Camalli, M.; Casciaro, G. L.; Giacovazzo, C.; Guagliardi, A.; Moliterni, A. G. G.; Polidori, G.; Spagna, R. *SIR97: A new program for solving and refining crystal structures*; Istituto di Cristallografia, CNR: Bari, Italy, 1999.
- (66) Sheldrick, G. M. *Acta Crystallogr.* **2008**, *A64*, 112–122.
- (67) (a) Parsons, S.; Gould, B.; Cooper, R.; Farrugia, L. ROTAX; University of Edinburgh: Edinburgh, Scotland, 2003; (b) Sheldrick, G. M. CELL\_NOW, version 2008/2; University of Göttingen: Göttingen, Germany, 2008.
- (68) Sheldrick, G. M. TWINABS, version 2008/4; University of Göttingen: Göttingen, Germany, 2008.
- (69) Spek, A. L. PLATON, version 300106; Utrecht University: Utrecht, The Netherlands, 2003.